Electrical Power and Energy Systems 146 (2023) 108710

Contents lists available at ScienceDirect

International Journal of Electrical Power and Energy Systems

journal homepage: www.elsevier.com/locate/ijepes

Model predictive control and protection of MMC-based MTDC power systems

Ajay Shetgaonkar *, Le Liu, Aleksandra Lekić, Marjan Popov, Peter Palensky

Intelligent Electrical Power Grids (IEPG-ESE), TU Delft, Delft, The Netherlands

ARTICLE INFO

Keywords:
Model predictive control
Wind power plant
GTFPGA
MMC
MTDC
VARC DC CB
Software-in-the-loop

ABSTRACT

Meshed offshore grids (MOGs) present a viable option for a reliable bulk power transmission topology. The station-level control of MOGs requires faster dynamics along with multiple objective functions, which is realized by the model predictive control (MPC). This paper provides control, and protection design for the Modular Multilevel Converter (MMC) based multi-terminal DC (MTDC) power system using MPC. MPC is defined using a quadratic cost function, and a dqz rotating frame voltage inputs are represented using Laguerre orthonormal functions. MPC has been applied for the control of both grid forming and grid following converters in a four-terminal MTDC setup, implemented for real-time Electromagnetic Transient (EMT) simulation. By applying numerous time-domain simulations, the advantages of the MPC when dealing with AC and DC side disturbances are investigated. The investigation highlights the MPC's inherent feature of fast response and high damping during- and post-disturbance, which is compared to the traditional PI controller performance. The analysis provides a comprehensive insight into the transient behavior of the MTDC during disturbances.

1. Introduction

In the past years, a significant amount of electrical energy from wind energy has been produced by Northern Europe's vast offshore wind parks [1–3]. However, its harnessing is followed by different challenges related to the social, economic, and technological levels. These challenges have already been addressed, and possible solutions were provided in the PROMOTioN project [4]. According to this project's results, HVDC MOGs need to be installed in the North Sea to meet the requirements related to climate changes and utilize Northern Europe's vast offshore wind energy. The MOGs can transfer offshore wind power between different countries. Besides, live wind gusts due to climate change, the onshore grid strength due to decommissioning of synchronous machines, and the load demands were not a matter of consideration in the previous large projects like Best Paths [5], and PROMOTioN [1].

The Energy conversion in MOGs is ensured by the power electronic devices (PEDs). PEDs are responsible for AC/DC and DC/AC energy transfer. They are controlled using fast controlling loops, which produce predicted and unpredicted high-frequency grid interactions [6,7], and are identified during Electromagnetic Transient (EMT) simulations. EMT simulations in real-time simulations (RTS) are preferred due to their Hardware-in-the-Loop (HiL) capabilities [8,9]. There is a need for a detailed model representation to identify the high-frequency interactions, which is possible by utilizing Field Programming Gate Arrays (FPGAs) [10]. Due to the penetration of power electronics, the power system response shifts from seconds to microseconds, and therefore, robust and fast non-linear controls like MPC are required [11–15]. Most of the proposed indirect MPCs or optimization control schemes for the power electronic applications make use of tool support to generate optimal control signals (online or offline) [16,17]. These tools consist of implicit function, and hence, disable the MPC algorithm to run on different real-time simulation platforms as they do not support a standalone code. In the Real-Time Digital Simulator (RTDS), for a low level control (i.e. proposed MPC), the modeling has to be done in C-code using C builder of RTDS. Furthermore, this C-code needs to be simple and executable in the given time step of $80\,\mu s$. The previous work of MPC has been focused on a single MMC unit in a real-time platform [13,18,19]. Furthermore, the application of MPC in MMC-based HVDC systems is implemented for offline EMT simulations [20,21]. A study on the three-terminal HVDC with an MPC on a real-time platform was carried out. However, this MPC design is centralized [22]. Hence, up to our knowledge, no study has been carried out with an MPC on a station level control for four-terminal HVDC grids with a standalone code in real-time. In this paper, we present an MPC algorithm that runs standalone in an RTDS environment and performance under faster transients. Further, interaction between MMC converter models (i.e. average and detailed MMC model) is investigated. This paper also proposes the live wind profile interface with the real time simulator.

The majority of high-frequency studies are carried out from the HVAC grid's perspective [23–26]. Some studies have also been carried

* Corresponding author.
E-mail address: A.D.Shetgaonkar@tudelft.nl (A. Shetgaonkar).

https://doi.org/10.1016/j.ijepes.2022.108710
Received 30 May 2022; Received in revised form 7 September 2022; Accepted 4 October 2022
Available online 29 October 2022
0142-0615/© 2022 The Author(s). Published by Elsevier Ltd. This is an open access article under the CC BY license (http://creativecommons.org/licenses/by/4.0/).

out from the HVDC grid perspective [27,28]. To provide full selective protection of the meshed HVDC system, a Direct Current Circuit Breaker (DC CB) is supposed to be applied at the end of each cable. However, among the different DC CBs [29], the Voltage source converter Assisted Resonant Current (VARC) DC CB has shown significant improvement during the initial transient interruption voltage (ITIV) with the fast operation (3 ms) at the kiloampere-current level [30]. Non-linear elements like surge arresters and voltage source converters (VSC) in VARC DC CBs can lead to unprecedented DC grid phenomena. These phenomena might arise during VARC DC CB's operation in the presence of a detailed MMC model and a linear MPC. In addition, these phenomena might also delay the post fault recovery of the DC grid. This paper also investigates the interaction between the non-linear control loops and active/passive HVDC network elements during different operating scenarios and transient events.

The dynamic behavior of improved control and protection (C&P) schemes for power systems, along with the stability and reliability of the meshed HVDC grid, is analyzed using the following RTS:

- Transients during nominal operation: The common cases under steady-state operation analyze set-point changes and switching operations.
- AC grid side fault analysis: The typical cases are chosen where symmetrical and asymmetrical faults occur.
- DC grid side fault analysis: The common cases analyze DC cable faults and internal converter station faults.

Furthermore, the performance and the interaction analysis of the MPC-controlled meshed HVDC grid are compared against the classical PI control-based meshed HVDC grid to provide interoperability scenarios. The outcome of these analyses will highlight the reliability and resilience of the designed MPC with fast recovery after the occurrence of small and large disturbances.

This paper is structured as follows. Section 2 describes the mathematical representation of MMC and MPC formulation for different control objectives. Section 3 describes the four-terminal HVDC system and the offshore wind power plant and its controls. The cross rack, Gigabit Transceiver Field Programmable Gate Array (GTFPGA) configuration, and the Software-in-the-loop (SiL) setup are described in Section 4. Section 5 deals with the performance of MPC and PI controllers during set-point changes, cable re-close, AC and DC side faults occurrence, and controller interoperability studies. Also, MMC's submodules' internal fault is analyzed for both controllers. Finally, Section 6 concludes the work and highlights the important findings.

2. MMC mathematical representation and MPC formulation

2.1. MMC state-space representation

The MMC is the three-phase rectifier/inverter that consists of 3 legs, one for each phase. Each leg consists of two arms, upper and lower arm, having N_{SM} half-bridge submodules.

The usual converter topology is depicted in Fig. 1. Variables from Fig. 1 are defined for all three phases, i.e. $j \in \{a, b, c\}$. Submodules (SMs) are considered with their averaged equivalents, R_{arm}, and L_{arm} being resistance and inductance, respectively. Each SM have capacitance C. The following equations for the voltage and the current can be written for the upper and lower arms:

$$v_{Mj}^{U,L} = m_j^{U,L} v_{Cj}^{U,L}, \qquad i_{Mj}^{U,L} = m_j^{U,L} i_j^{U,L}, \tag{1}$$

where $m_j^{U,L}$ are the corresponding upper and lower arm insertion indices.

The converter model is developed following the methodology reported in [31]. Using the $\Sigma - \Delta$ nomenclature, the variables in the upper and lower converter arms can be represented as:

$$i_j^{\Delta} = i_j^U - i_j^L, \quad i_j^{\Sigma} = \frac{i_j^U + i_j^L}{2}, \tag{2a}$$

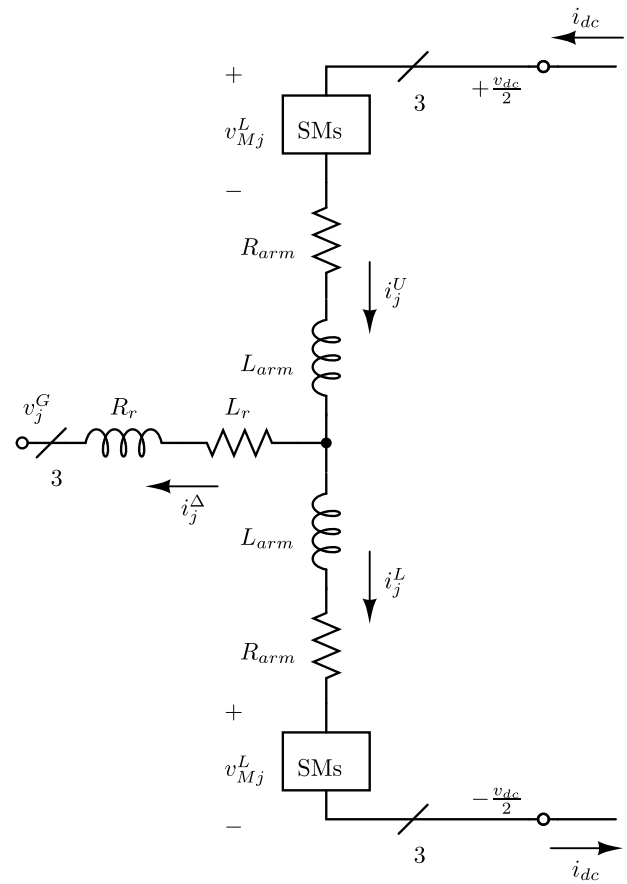

Fig. 1. MMC diagram.

$$v_{Cj}^{\Delta} = \frac{v_{Cj}^U - v_{Cj}^L}{2}, \quad v_{Cj}^{\Sigma} = \frac{v_{Cj}^U + v_{Cj}^L}{2}, \tag{2b}$$

$$m_j^{\Delta} = m_j^U - m_j^L, \quad m_j^{\Sigma} = m_j^U + m_j^L, \tag{2c}$$

$$v_{Mj}^{\Delta} = \frac{-v_{Mj}^U + v_{Mj}^L}{2} = -\frac{m_j^{\Delta} v_{Cj}^{\Sigma} + m_j^{\Sigma} v_{Cj}^{\Delta}}{2}, \tag{2d}$$

$$v_{Mj}^{\Sigma} = \frac{v_{Mj}^U + v_{Mj}^L}{2} = \frac{m_j^{\Sigma} v_{Cj}^{\Sigma} + m_j^{\Delta} v_{Cj}^{\Delta}}{2}. \tag{2e}$$

By making use of the dqz-frame [31,32], the set of differential equations can be written with capacitor voltages and inductor currents as state variables:

$$\frac{d}{dt}\left(\vec{i}_{dq}^{\Delta}\right) = \frac{\vec{v}_{Mdq}^{\Delta} - \left(\omega L_{eq}^{ac} J_2 + R_{eq}^{ac} I_2\right)\vec{i}_{dq}^{\Delta} - \vec{v}_{dq}^{G}}{L_{eq}^{ac}}, \tag{3a}$$

$$\frac{d}{dt}\left(\vec{i}_{dq}^{\Sigma}\right) = -\frac{\vec{v}_{Mdq}^{\Sigma} + \left(R_{arm} I_2 - 2\omega L_{arm} J_2\right)\vec{i}_{dq}^{\Sigma}}{L_{arm}}, \tag{3b}$$

$$\frac{d}{dt}\left(i_z^{\Sigma}\right) = \frac{v_{dc}}{2L_{arm}} - \frac{v_{Mz}^{\Sigma} + R_{arm}\, i_z^{\Sigma}}{L_{arm}}, \tag{3c}$$

$$\frac{d}{dt}\left(\vec{v}_{Cdq}^{\Delta}\right) = \frac{N_{SM}}{2C}\vec{i}_{Mdq}^{\Delta} - \omega J_2 \vec{v}_{Cdq}^{\Delta}, \tag{3d}$$

$$\frac{d}{dt}\left(\vec{v}_{CZ_{dq}}^{\Delta}\right) = -\frac{N_{SM}}{8C}\Psi - 3\omega J_2 \vec{v}_{CZ_{dq}}^{\Delta}, \tag{3e}$$

$$\frac{d}{dt}\left(\vec{v}_{Cdqz}^{\Sigma}\right) = \frac{N_{SM}}{2C}\vec{i}_{Mdqz}^{\Sigma} + 2\omega J_3 \vec{v}_{Cdqz}^{\Sigma}, \tag{3f}$$

where N_{SM} is the number of SMs per arm, and ω is the angular frequency, and:

$$\vec{i}_{Mdq}^{\Delta} = P_{\omega}(t)\left(P_{-2\omega}^{-1}(t)\,\vec{m}_{dqz}^{\Sigma} \circ \frac{P_{\omega}^{-1}(t)\,\vec{i}_{dqz}^{\Delta}}{2} + P_{\omega}^{-1}(t)\,\vec{m}_{dqz}^{\Delta} \circ P_{-2\omega}^{-1}(t)\;\vec{i}_{dqz}^{\Sigma}\right),$$

$$\vec{i}_{Mdqz}^{\Sigma} = P_{-2\omega}(t)\left(P_{-2\omega}^{-1}(t)\,\vec{m}_{dqz}^{\Sigma} \circ P_{-2\omega}^{-1}(t)\;\vec{i}_{dqz}^{\Sigma} + P_{\omega}^{-1}(t)\;\vec{m}_{dqz}^{\Delta} \circ \frac{P_{\omega}^{-1}(t)\;\vec{i}_{dqz}^{\Delta}}{2}\right),$$

$$\vec{v}^{\Delta}_{Mdqz} = -\frac{P_{\omega}(t)}{2}\left(P^{-1}_{\omega}(t)\,\vec{m}^{\Delta}_{dqz}\circ P^{-1}_{-2\omega}(t)\,\vec{v}^{\Sigma}_{Cdqz} + P^{-1}_{-2\omega}(t)\,\vec{m}^{\Sigma}_{dqz}\circ P^{-1}_{\omega}(t)\,\vec{v}^{\Delta}_{Cdqz}\right),$$

$$\vec{v}^{\Sigma}_{Mdq} = -\frac{P_{-2\omega}(t)}{2}\left(P^{-1}_{\omega}(t)\,\vec{m}^{\Delta}_{dqz}\circ P^{-1}_{\omega}(t)\,\vec{v}^{\Delta}_{Cdqz} + P^{-1}_{-2\omega}(t)\,\vec{m}^{\Sigma}_{dqz}\circ P^{-1}_{-2\omega}(t)\,\vec{v}^{\Sigma}_{Cdqz}\right),$$

$$\Psi = \begin{bmatrix} i^{\Delta}_d m^{\Sigma}_d + 2i^{\Sigma}_d m^{\Delta}_d + i^{\Delta}_q m^{\Sigma}_q + 2i^{\Sigma}_q m^{\Delta}_q + 4i^{\Sigma}_z m^{\Delta}_{Zd} \\ i^{\Delta}_q m^{\Sigma}_d + 2i^{\Sigma}_d m^{\Delta}_q - i^{\Delta}_d m^{\Sigma}_q - 2i^{\Sigma}_q m^{\Delta}_d + 4i^{\Sigma}_z m^{\Delta}_{Zq} \end{bmatrix},$$

with $L^{ac}_{eq} = L_r + \frac{L_{arm}}{2}$, $R^{ac}_{eq} = R_r + \frac{R_{arm}}{2}$. Here, the $P_{\omega_0}(t) = \frac{2}{3}\begin{bmatrix} \cos(\omega_0 t) & \cos\left(\omega_0 t - \frac{2\pi}{3}\right) & \cos\left(\omega_0 t - \frac{4\pi}{3}\right) \\ \sin(\omega_0 t) & \sin\left(\omega_0 t - \frac{2\pi}{3}\right) & \sin\left(\omega_0 t - \frac{4\pi}{3}\right) \\ \frac{1}{2} & \frac{1}{2} & \frac{1}{2} \end{bmatrix}$ and $P^{-1}_{\omega_0}(t) = \frac{3}{2}P^{T}_{\omega_0}(t) + \frac{1}{2}\begin{bmatrix} 0 & 0 & 1 \\ 0 & 0 & 1 \\ 0 & 0 & 1 \end{bmatrix}$ are the Park's transformation and inverse park's transformation at ω_0 angular frequency and $\omega_0 \in \{-2\omega, \omega, 3\omega\}$. I_n is the identity matrix with an order of $n \times n$, while matrices $J_2 = \begin{bmatrix} 0 & 1 \\ -1 & 0 \end{bmatrix}$, and $J_3 = \begin{bmatrix} 0 & 1 & 0 \\ -1 & 0 & 0 \\ 0 & 0 & 0 \end{bmatrix}$. In the previous equations, $(\vec{\cdot})$ denotes a vector and the $(\circ)$ is a hadamard product. Subscripts d, q, z denote the corresponding components within the dqz-frame at the angular frequency ω, while Z_{dq} represents zero component separated to d and q components in the reference frame determined with the angular frequency 3ω.

In the further text, the MMC's AC side and DC side dynamics given in Eq. (3) is discretized using the zero-order hold discretization method and augmented in the rate based state space equations [32]:

$$\begin{bmatrix} \Delta\vec{x}(k+1) \\ \vec{y}(k+1) \end{bmatrix} = \overbrace{\begin{bmatrix} F(T_s) & o^T \\ H(T_s)F(T_s) & 1 \end{bmatrix}}^{A_d}\overbrace{\begin{bmatrix} \Delta\vec{x}(k) \\ \vec{y}(k) \end{bmatrix}}^{\vec{x}_m(k)} + \overbrace{\begin{bmatrix} G(T_s) \\ H(T_s)G(T_s) \end{bmatrix}}^{B_d}\Delta\vec{u}(k), \tag{4a}$$

$$\vec{y}_m(k) = \overbrace{\begin{bmatrix} 0 & I \end{bmatrix}}^{C_d}\vec{x}_m(k), \tag{4b}$$

where $H(T_s)$ is an identity matrix, whereas $F(T_s) = e^{A\,T_s}$ and $G(T_s) = A^{-1}\left(e^{A\,T_s} - I\right)B$. Matrices A and B are determined from the continuous system equations and they are separately defined for each MPC as shown in Sections 2.3 and 2.4. T_s is the sampling time, and it is set to 30 μs. Furthermore, the augmented state is defined as $\Delta\vec{x}(k) = \vec{x}(k) - \vec{x}(k-1)$, where $\vec{x}(k)$ indicates the system state vector at kth instant and $\vec{x}(k-1)$ indicates vector of past states. Similarly, the augmented input is defined as $\Delta\vec{u}(k) = \vec{u}(k) - \vec{u}(k-1)$, where $\vec{u}(k)$ represent the system inputs at kth instant and $\vec{u}(k-1)$ indicates the past inputs.

2.2. MPC formulation

In power electronic applications, the MPC has been classified into two major categories: indirect (also known as continuous control set MPC) and direct MPC. The direct MPC creates the firing sequences and has a high degree of control. However, MMC has a few hundred submodules, and creation of firing pulses would result in an extremely high computation burden during real-time simulation.

The indirect MPC controls the converter by making use of the modulator which converts the reference signal into the firing sequences. Furthermore, the indirect MPC is classified into explicit and implicit MPC. Implicit MPC solves the optimization problem online at each time step. In comparison, the explicit MPC make use of offline optimization techniques. Furthermore, an outline of the MPC implemented in the HVDC application are provided in Table 1.

Here, we present implicit MPC. The implicit MPC in literature for HVDC application usually uses the difference of the control signal, (i.e. Δu). The use of Δu in the cost function with the high sampling rate, and high demands on close-loop performance requires a large number of parameters (i.e. control horizon N_c). This further creates poorly numerically conditioned solutions and high computation power.

Thus, in this subsection we will explain Laguerre network representation which approximates Δu. In the Laguerre based MPC design, the $\Delta U = [\Delta u(k_i)\ \Delta u(k_i+1) \cdots\ \Delta u(k_i+N_c-1)]^T$ can be represented by pulse operator (i.e. $\delta(i)$) in conjunction with ΔU and N_c is control horizon. As a result, $\Delta u(k_i+1) = \left[\delta(i)\ \delta(i-1)\ \cdots\ \delta(i-N_c+1)\right]$, where the pulse operator is defined as

$$\delta(i) = \begin{cases} 1, & i = 0, \\ 0, & i \neq 0. \end{cases}$$

Therefore, the presented MPC results in a lower number of parameters and lower computation burden during online optimization [47].

By considering the discrete augmented system

$$\vec{x}_{\vec{m}}(k+1) = A_d\vec{x}_{\vec{m}}(k) + B_d\Delta\vec{u}(k), \tag{5}$$

with state variables $\vec{x_m}$, inputs $\vec{u}$, for kth instance. Matrices A_d and B_d, with subscript d denoting a discrete system, contain corresponding quantities. Inputs $\Delta\vec{u}(k)$ are represented using orthonormal Laguerre functions [32,47]. The removal of the dependency of the control horizon gives an advantage for the real-time applications, as the number of parameters is reduced. With Laguerre's function, the control parameter changes to $\vec{\eta}$ from $\Delta\vec{u}(k)$:

$$\Delta\vec{u}(k+m|k) = \begin{bmatrix} L_1(m)^T & o^T_1 & \cdots & o^T_M \\ o^T_1 & L_2(m)^T & \cdots & o^T_M \\ \vdots & \vdots & \ddots & \vdots \\ o^T_1 & o^T_2 & \cdots & L_M(m)^T \end{bmatrix}\vec{\eta} \tag{6}$$

where o^T_k represents zero block raw vector with an identical dimension to $L_k(m)^T$. The vector $L(k) = [l_1(k), l_2(k), \ldots, l_N(k)]^T$, and $l_i(k)$ is the discrete Laguerre function determined by the inverse z transformation of $\Gamma_i(z)$. Function in Z-domain $\Gamma(z)$ is defined as $\Gamma_i(z) = \Gamma_{i-1}(z)\frac{z^{-1}-a}{1-az^{-1}}$, and $\Gamma_1(z) = \frac{\sqrt{1-a^2}}{1-az^{-1}}$. Here, a is called Laguerre's network pole with $0 < a < 1$ for safeguarding the network's stability, $\beta = \sqrt{1-a^2}$, and N is the number of terms required to represent the approximated system response. The notation $\vec{f}(k+m|k)$ is a discrete value of the vector $\vec{f}$ at the instance $k+m$ estimated during sampling instant k. Furthermore, it is

$$L(k+1) = A_l L(k), \tag{7a}$$

$$A_l = \begin{bmatrix} a & 0 & 0 & 0 \\ \beta & a & 0 & 0 \\ -a\beta & \beta & a & 0 \\ \vdots & \vdots & \vdots & \ddots \end{bmatrix}, \tag{7b}$$

$$L(0)^T = \sqrt{\beta}\begin{bmatrix} 1 & -a & a^2 & \cdots & (-1)^{N-1}a^{N-1} \end{bmatrix}, \tag{7c}$$

$$\vec{\eta} = \begin{bmatrix} c_1 & c_2 & \cdots & c_N \end{bmatrix}^T, \tag{7d}$$

The value of η is calculated by minimizing the objective (cost) function, subjected to the equality and inequality constraints. The cost function is formulated considering LQR as a base. Hence, the cost function is given by

$$\min_{\vec{\eta}}\ J = \sum_{i=1}^{N_p}\vec{x}_{\vec{m}}(k+i|k)^T Q\vec{x}_{\vec{m}}(k+i|k) + \vec{\eta}^T R\vec{\eta}, \tag{8a}$$

$$\text{subject to } M\vec{\eta} \leq b, \tag{8b}$$

$$\vec{x}_{\vec{m}}(k+i|k) = \vec{r}(k) - \vec{y}_m(k|k). \tag{8c}$$

Here, $Q \succeq 0$ and $R \succ 0$ are weighting matrices, and N_p is the prediction horizon. For variables $\vec{x}_{\vec{m}}(k)$, vector $r(k)$ is a reference signal. The Matrix

Table 1
Overview of the MPC for HVDC application.

Literature	MPC problem[a]	Platform	Online solver	Circuit
J. Qin et al. [33]	$J = Q\left\|y_{ref}(k+1) - y(k+1)\right\|_1$	PSCAD/EMTDC	No	Point to point HVDC
D. Zhou et al. [34]	$J = Q\left\|y_{ref}(k+1) - y(k+1)\right\|_1$	dSPACE	No	Grid connected MMC unit.
J. Bocker et al. [35]	$J = Q\left\|y_{ref}(k+1) - y(k+1)\right\|_1 + Ru\left\|u_{(k)} - u(k-1)\right\|_1$	Scaled converter test bench.	No	Grid connected MMC unit.
A. Dekka et al. [36]	$J = Q\left\|y_{ref}(k+1) - y(k+1)\right\|_1$	MATLAB/Simulink simulations / dSPACE	No	Grid connected MMC unit.
M. Vatani et al. [37]	$J = Q\left\|y_{ref}(k+1) - y(k+1)\right\|_1$	PSCAD/EMTDC	No	Grid connected MMC unit.
P. Liu et al. [38]	$J = Q\left\|y_{ref}(k+1) - y(k+1)\right\|_1$	MMC Back-to-back dynamic test system	No	Back-to-back MMC-HVDC system.
J. W. Moon et al. [39]	$J = Q\left\|y_{ref}(k+1) - y(k+1)\right\|_1$	PSCAD/EMTDC	No	Grid connected MMC unit.
Y. Wang Yue et al. [40]	$J = Q\left\|y_{ref}(k+1) - y(k+1)\right\|_1$	PSCAD/EMTDC	No	Grid connected MMC unit.
J. Huang et al. [41]	$J = Q\left\|y_{ref}(k+1) - y(k+1)\right\|_1$	PSCAD/EMTDC & experimental prototype	No	Grid connected MMC unit.
H. Mahmoudi et al. [42]	$J = Q\left\|y_{ref}(k+1) - y(k+1)\right\|_1$	DSP/ prototype MMC	No	Grid connected MMC unit.
T. Nowak et al. [43]	$J = Q\left\|y_{ref}(k+1) - y(k+1)\right\|_1 + Ru\left\|u_{(k)} - u(k-1)\right\|_1$	PSCAD/EMTDC	No	Multi-terminal HVDC system
J. Zhang et al. [44]	$J = Q\left\|y_{ref}(k+1) - y(k+1)\right\|_1$	PSCAD/EMTDC	No	Point to point HVDC
S. Pirooz Azad et al. [45]	$J = Q\left\|y_{ref}(k+1) - y(k+1)\right\|_2 + Ru\left\|u_{(k)} - u(k-1)\right\|_2$	PSCAD/EMTDC	Quadratic	Meshed IEEE 14-bus with HVDC link.
P. Mc Namara et al. [45]	$J = Q\left\|y_{ref}(k+1) - y(k+1)\right\|_2 + Ru\left\|u_{(k)} - u(k-1)\right\|_2$	Matlab /Simulink	Quadratic	A multi-terminal DC grid.
S. Fuchs et al. [46]	$J = Q\left\|y_{ref}(k+1) - y(k+1)\right\|_2 + Ru\left\|u_{(k)} - u(k-1)\right\|_2$	Matlab/Simulink	Quadratic	Grid-connected MMC unit.
M. M. Belhaouanes et al. [22]	$J = Q\left\|y_{ref}(k+1) - y(k+1)\right\|_2 + Ru\left\|u_{(k)} - u(k-1)\right\|_2$	Matlab/Simulink and OPAL-RT	Quadratic	Three-terminal VSC-HVDC

[a] Q, R are weight matrices for output and control states, $y_{ref}(k+1)$, $y(k+1)$ are reference and predicted output and $u(k)$, $u(k-1)$ are the present and past control inputs.

M and the column vector b are related to the constraint information on the rate and amplitude:

$$M = \begin{bmatrix} M_{\Delta U} & o & o & o \\ o & M_{\Delta U} & o & o \\ o & o & -M_U & o \\ o & o & o & -M_U \end{bmatrix},$$

$$b = \begin{bmatrix} \Delta U_{max} \\ -\Delta U_{max} \\ U_{max} - \vec{u}(k-1) \\ -U_{min} + \vec{u}(k-1) \end{bmatrix},$$

$$M_{\Delta U} = \begin{bmatrix} L_1(m)^T & o & \cdots & o \\ o & L_2(m)^T & \cdots & o \\ \vdots & \vdots & \ddots & \vdots \\ o & o & \cdots & L_m(m)^T \end{bmatrix},$$

$$M_U = \begin{bmatrix} \sum_{i=0}^{N-1} L_1(i)^T & o & \cdots & o \\ o & \sum_{i=0}^{N-1} L_2(i)^T & \cdots & o \\ \vdots & \vdots & \ddots & \vdots \\ o & o & \cdots & \sum_{i=0}^{N-1} L_m(i)^T \end{bmatrix},$$

$$\Delta U_{max} = 1 \times \vec{1}, \qquad \Delta U_{min} = -1 \times \vec{1},$$
$$U_{max} = 0.8 \times \vec{1}, \qquad U_{min} = -0.8 \times \vec{1},$$

where $\vec{1}$ is the vector of all ones with dimensions $N \times 1$, and m indicates the future sampling instant. Since the formulation of MPC is in per unit, the values of constraints $\Delta U_{max,min}$ and $U_{max,min}$ set based on the performance and control energy. In this paper, we allow control energy of inner and grid forming MPC up to 80% of rated voltage such that modulation index remains below 1.2 pu. Further, this limit has an impact on the arm current during the fault. Furthermore, taking the performance into the consideration, the rate constraints are kept equal to 1 pu.

In the unconstrained case, Eq. (8b) does not exist, and the optimization problem is only solved by using a terminal constraint. The quadratic programming problem (8) is solved by making use of Hildreth's quadratic programming procedure [47].

MPC given with Eq. (8) is stable, which can be shown by taking into account the terminal constraint $\vec{x}(k+N_p|k) = 0$, see chapter 3 in [47]. If it is assumed that for every k exists $\vec{\eta}$ which satisfies (8a) subjected to terminal constraint, the stability can be expressed by using Lyapunov function:

$$V(\vec{x}(k), k) = \sum_{i=1}^{N_p} \vec{x}(k+i|k)^T Q \vec{x}(k+i|k) + \sum_{i=1}^{N_p-1} \Delta\vec{u}(k+i)^T R \Delta\vec{u}(k+i).$$

This Lyapunov function equivalents the cost expressed by (8a). The equality stems from the fact that $\Delta\vec{u}(k+i) = L(i)^T\vec{\eta}(k) = [l_1(i), \ldots, l_N(i)]^T\vec{\eta}(k)$, and that the convolution between Laguerre functions gives:

$$\sum_{m=0}^{N_p} l_i(m) l_j(m) = \begin{cases} 0 & \text{for } i \neq j, \\ 1 & \text{for } i = j. \end{cases}$$

The Lyapunov function for the next sampling instant $k+1$ is:

$$V(\vec{x}(k+1), k+1) = \sum_{i=1}^{N_p} \vec{x}(k+i+1|k+1)^T Q \vec{x}(k+i+1|k+1) + \sum_{i=1}^{N_p-1} \Delta\vec{u}(k+i+1)^T R \Delta\vec{u}(k+i+1). \tag{11}$$

Then, because of the optimality of the solution for $\vec{\eta}$, the following inequality holds $V(\vec{x}(k+1), k+1) \leq \overline{V}(\vec{x}(k+1), k+1)$, for $\overline{V}(\vec{x}(k+1), k+1)$ which is similar to $V(\vec{x}(k+1), k+1)$, where the original control sequence (i.e. $L(0)^T\eta^k$, $L(1)^T\eta^k$, $\ldots$, $L(N_p-1)^T\eta^k$) is

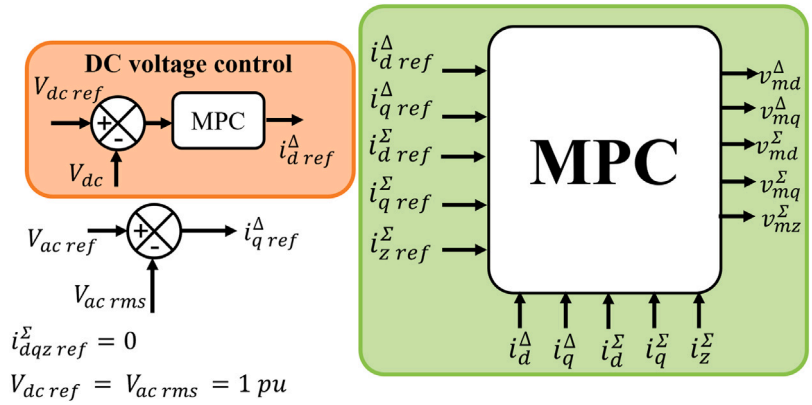

Fig. 2. Graphical representation of the cascaded MPC DC voltage controller: left — outer MPC and right — inner MPC controller.

replaced by the sequence $L(1)^T\eta^k,\ L(2)^T\eta^k,\ \ldots,\ L(N_p-1)^T\eta^k,\ 0$. Therefore, $\overline{V}(\vec{x}(k+1),k+1)$ shares the same control sequence as $V(\vec{x}(k),k)$ for the sample time $k+1,\ k+2,\ \ldots,\ k+N_p-1$. To prove that the system is stable, it is sufficient to show that the forward difference of the discrete Lyapunov function is negative. In the unconstrained case, this can be shown using terminal constraint [47]:

$$V(\vec{x}(k+1),k+1)-V(\vec{x}(k),k)\le \overline{V}(\vec{x}(k+1),k+1)-V(\vec{x}(k),k)=$$
$$0,\ \text{terminal constraint}$$
$$=\overbrace{\vec{x}(k+N_p|k)^TQ\vec{x}(k+N_p|k)}-\vec{x}(k+1)^TQ\vec{x}(k+1)-\Delta\vec{u}(k)^TR\Delta\vec{u}(k)=$$
$$=-\vec{x}(k+1)^TQ\vec{x}(k+1)-\Delta\vec{u}(k)^TR\Delta\vec{u}(k)<0.$$

Clearly, the system is stable. In the constrained case, the stability is proven using Eq. (8b).

2.3. Cascaded MPC for DC voltage control

The MPC is designed using two cascaded controllers: inner and outer MPC. The inner MPC is used to control the MMC's currents, while the output sets the DC voltage, as it is depicted in Fig. 2. This control architecture is similar to conventional PI control as given in [48]. Both controllers, the inner and outer MPC, control the discretized augmented system defined by the difference Eqs. (5).

The DC voltage dynamics are in general related to the power grid dynamics, which could be unknown and hard to be modeled. Thus, sometimes is hard to have an accurate model. In that case is possible to use model mismatch factor, as it is described in Appendix.

2.3.1. Inner MPC loop

The inner MPC loop is represented in the discretized augmented form as in (4), with state matrix A_d, input matrix B_d and output matrix C_d. Matrices A and B are taken from a continuous averaged system representation of the MMC as in (3) and written as :

$$A=\begin{bmatrix} -\frac{R_{arm}}{L_{arm}} & 2\omega & 0 & 0 & 0\\ -2\omega & -\frac{R_{arm}}{L_{arm}} & 0 & 0 & 0\\ 0 & 0 & -\frac{R_{arm}}{L_{arm}} & 0 & 0\\ 0 & 0 & 0 & -\frac{R^{ac}_{eq}}{L^{ac}_{eq}} & -\omega\\ 0 & 0 & 0 & \omega & -\frac{R^{ac}_{eq}}{L^{ac}_{eq}}\end{bmatrix}, \tag{12a}$$

$$B=\text{diag}\left\{-\frac{1}{L_{arm}},-\frac{1}{L_{arm}},-\frac{1}{L_{arm}},\frac{1}{L^{ac}_{eq}},\frac{1}{L^{ac}_{eq}}\right\}, \tag{12b}$$

The vector $\vec{x}=[i^{\Sigma}_d,\ i^{\Sigma}_q,\ i^{\Sigma}_z,\ i^{\Delta}_d,\ i^{\Delta}_q]^T$ represents state variables, while $\vec{u}=[v^{\Sigma}_{Md},\ v^{\Sigma}_{Mq},\ v^{\Sigma}_{Mz}-\frac{v_{dc}}{2},\ v_{Md}-v^{\Delta}_d,\ v_{Mq}-v^{\Delta}_q]^T$ represents system inputs. Therefore, upon discretization and augmentation (Eq. (4)), $\vec{x}_{\vec{m}}=[\Delta\vec{x},i^{\Sigma}_{d\ ref}-i^{\Sigma}_d,\ i^{\Sigma}_{q\ ref}-i^{\Sigma}_q,\ i^{\Sigma}_{z\ ref}-i^{\Sigma}_z,\ i^{\Delta}_{d\ ref}-i^{\Delta}_d,\ i^{\Delta}_{q\ ref}-i^{\Delta}_q]^T$ represents the state variables. Here, the output variables are the same as the state variables.

This MPC loop controls the circulating and output currents, as shown in Fig. 2 right. In order to minimize the circulating currents, the references of Σ-currents ($\vec{i}^{\Sigma}_{dqz\ ref}$) are set to zero. The references of Δ-currents ($\vec{i}^{\Delta}_{dq\ ref}$) are provided by the outer MPC loop, and the reactive power or AC voltage support control.

2.3.2. Outer MPC loop

This MPC loop is used to control the DC voltage. It is designed as the outer loop to ensure that the rated DC voltage is maintained dynamically, i.e., without linearization. Thus, the outer loop is added to consider other system variables, which are indirectly derived by the inner MPC loop state variables. The continuous state space matrices are:

$$A=\left[\frac{-1}{k_{dc}\times T_{dc}}\right],\quad B=\left[\frac{1}{k_{dc}}\right]. \tag{13}$$

The vector $\vec{x}=[v_{dc\ ref}-v_{dc}]$ represents the state variables, while $\vec{u}=\left[i^{\Delta}_{d,ref}\right]$ represents system inputs. The k_{dc} and T_{dc} are 6.5 and 0.0035, respectively. This is further discretized and augmented to form Eq. (4). Upon discretization and augmentation, $\vec{x}_{\vec{m}}=[\Delta\vec{x},v_{dc\ ref}-v_{dc}]^T$ represents state variables. Here, the output variables are the same as the state variables. The cost function minimizes the control signal to eliminate any deviation from the rated DC link voltage. The rate constraint is responsible for damping, and damping is better when the rate constraint is larger. Thus, the input rate and amplitude constraints are set to 5 and 0.8, respectively.

2.4. Grid forming MPC

The grid forming control is based on the direct Voltage ($V_{ac}-f$) control [49]. The state equation for the grid forming MPC is represented by matrices:

$$A=\begin{bmatrix}\frac{-1}{k_{GF}\times T_{GF}} & 0 & 0 & 0\\ 0 & -\frac{R_{arm}}{L_{arm}} & 2\omega & 0\\ 0 & -2\omega & -\frac{R_{arm}}{L_{arm}} & 0\\ 0 & 0 & 0 & -\frac{R_{arm}}{L_{arm}}\end{bmatrix}, \tag{14a}$$

$$B=\text{diag}\left\{\frac{1}{k_{GF}},-\frac{1}{L_{arm}},-\frac{1}{L_{arm}},-\frac{1}{L_{arm}}\right\}, \tag{14b}$$

and vector $\vec{x}=[v_{ac\ ref}-v_{ac},\ i^{\Sigma}_d,\ i^{\Sigma}_q,\ i^{\Sigma}_z]^T$ represents the state variables, while $\vec{u}=[v^{\Delta}_{Md},\ v^{\Sigma}_{Md},\ v^{\Sigma}_{Mq},v^{\Sigma}_{Mz}-\frac{v_{dc}}{2}]$ represents system inputs. The k_{GF} and T_{GF} are 6.5 and 0.008, respectively. Upon discretization and augmentation as shown in Eq. (4), $\vec{x}_m=[\Delta\vec{x},\ v_{ac\ ref}-v_{ac},\ i^{\Sigma}_{d\ ref}-i^{\Sigma}_d,\ i^{\Sigma}_{q\ ref}-i^{\Sigma}_q,\ i^{\Sigma}_{z\ ref}-i^{\Sigma}_z,\ ]^T$ represents state variables. Here, the

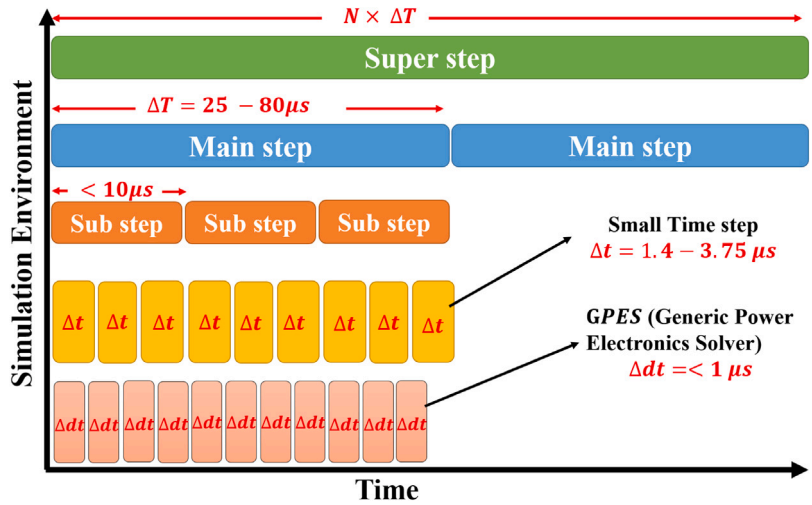

Fig. 3. Different simulation step in RTDS, $N = 2 - 5$.

output variables are the same as the state variables. The cost function minimizes the control signal to eliminate any deviation from the rated AC voltage at the point of common coupling (PCC) of offshore AC grid and minimize the circulating current in the converter.

3. System configuration of the four-terminal HVDC system

Among different real-time simulators, the RTDS is widely used in academia and industry. The RISC processor of NovaCor in RTDS consists of ten cores (CPU units), which operate at 3.5 GHz each. In the RTDS, there are different simulation time steps as shown in Fig. 3. Each modeling time step has its advantages and disadvantages. Typically, for every simulation, three components exist in RTDS, namely, the *Network solution*, *Control*, and *Power system*. Among these components, the *Power system* changes with the type of simulation time step model (i.e. super step, main step, etc.). The *control* works in the main step. Thus, the execution of all *control* units has to be done within 80 μs. For a large system, the *control* can be split into several parallel paths. However, this parallel path is restricted to the number of available cores in RTDS.

Considering all these requirements, the users have defined MPC's execution time within the 80 μs to run successfully in the real-time simulator. Among the different MPC schemes [50], OVL-MPC provides the best performance for HVDC application [50]. Other MPC schemes can also be implemented within RTDS environment; however, a trade-off between the predictive plant model and prediction horizon must be made. Still, up to now, we are not aware of an MPC within the RTDS environment.

Among the OVL-MPC, MPC-based on Laguerre's function is the most suitable for a real-time application due to the independence of the control horizon. However, this type of MPC was used only in electrical drives. The applications for MMC-based HVDC power systems have not been studied.

Fig. 4 depicts a ±200 kV monopole meshed four-terminal MMC-based HVDC power system with a digital twin model of a 2 GW offshore wind farm. This power system is applied to test the accuracy of the proposed control and protection algorithms. In the system of Fig. 4, two offshore wind farms operate at different wind speeds. The wind speed data is taken directly from the actual measurement in the North Sea. The wind speed measurements are updated into the RTDS every two seconds using the SiL setup. There are three detailed equivalent MMC models (MMCs 1, 2, and 4), implemented using GTFPGAs, and one averaged model of the MMC (MMC 3), implemented in the RTDS core.

Furthermore, MMC 1 is connected to the strong grid, modeled as a Thevenin grid equivalent. MMC 3 is connected to the weak grid modeled as a Thevenin grid equivalent with a lower Short Circuit Ratio (SCR). The offshore MMCs act as grid forming converters. The data of the four-terminal HVDC system is shown in Table 2. The MTDC system has five cables with the lengths of each 200 km. The VARC DC CB is implemented at both ends of the cable as shown in Fig. 4.

Table 2
Data of the four-terminal MTDC.

Parameter	Converters			
	MMC 1	MMC 2	MMC 3	MMC 4
Active power	500 MW	500 MW	500 MW	500 MW
Control mode	Vdc	Vac	PQ	Vac
Reactive power	0 MVAR	0 MVAR	0 MVAR	0 MVAR
DC link Voltage	±200 kV			
Rated power	800 MW			
Number of Submodules per arm	200			
Arm capacitance Carm	22 μF			
Arm inductance Larm	42 mH			
Arm resistance Rarm	0.544 Ω			
AC converter voltage	220 kV			
Transformer leakage reactance	0.18 pu			
Onshore AC grid				
Onshore grid 1		Onshore grid 2		
AC grid voltage	380 kV	AC grid voltage	380 kV	
SCR	37.5	SCR	3	
Offshore AC grid				
AC grid voltage	145 kV			

3.1. Model of MMCs and their controls

The switching model of the MMC is implemented on a Xilinx VC707 FPGA (Virtex 7 FPGA), called GTFPGA within firmware for RTDS connection, that satisfies high computational requirements. The MMC's operation (i.e. its equations) is solved with a time-step of 1.4 to 3 μs, which is known as a small-time step. A GTFPGA unit [51] is used to represent one leg of the MMC. Thus a total of three GTFPGA units are required to represent one MMC unit. Additionally, the sub-module capacitor voltage balancing controller is required. Due to the high number of submodules, this controller is implemented using two GTFPGA units. The connections between RTDS and GTFPGAs, as well as between GTFPGAs, are realized by two full-duplex fiber optic cables using the Aurora protocol. To represent three detailed MMCs (MMCs 1, 2, and 4), nine GTFPGAs are used for MMC units' legs. Furthermore, six GTFPGAs are used to represent the submodule capacitor voltage balancing controllers for respective MMC units. In total, fifteen GTFPGAs

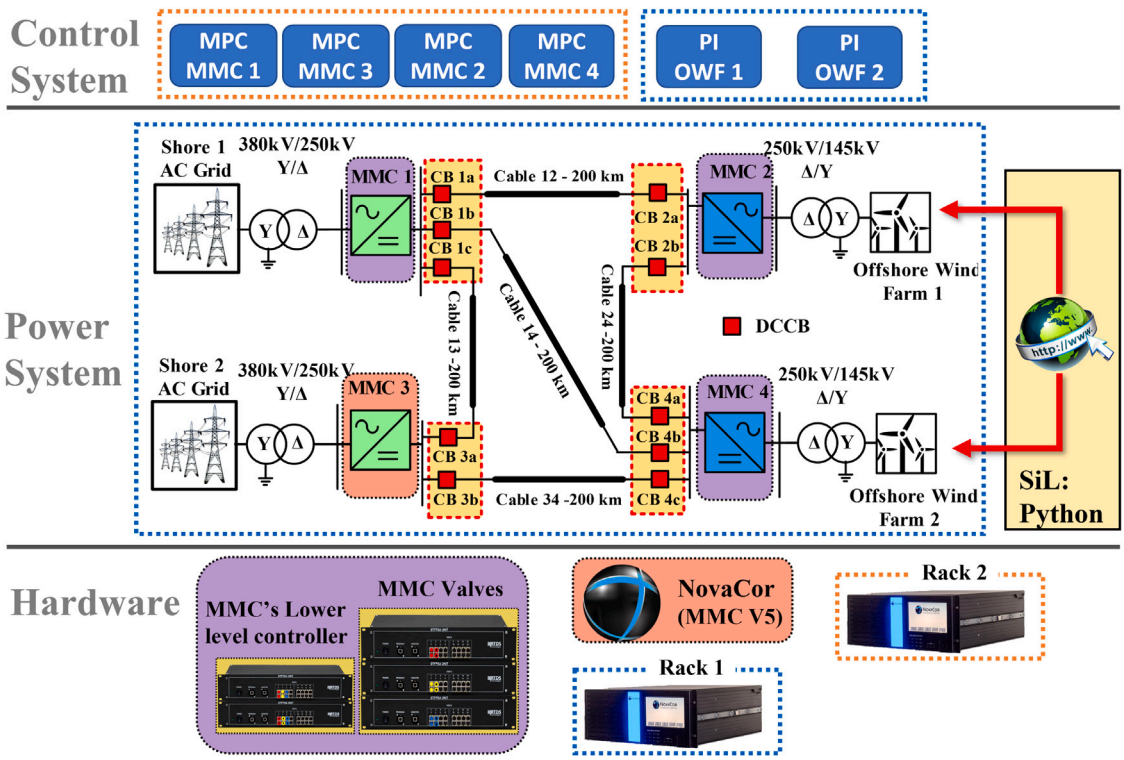

Fig. 4. The four-terminal MMC-based MTDC system with a HiL and a SiL setup.

Table 3
Values for PI control.

	MMC 1	MMC 2	MMC 3	MMC 4
Outer Voltage loop				
Proportional constant (k_p)	8 pu	–	8 pu	–
Integral Time constant (T)	0.2 s	–	0.2 s	–
Inner current loop				
Proportional constant (k_p)	0.48 pu	0.2 pu	0.48 pu	0.2 pu
Integral constant (T)	0.0067 s	0.0333 s	0.0067 s	0.0333 s

are used. Each valve of the MMC is represented as a surrogate network in RSCAD/RTDS. The surrogate network has four sections. Namely, the Reactor section, Block section, + ve inserted submodules (SM) section, and a Bypass section. The reactor, the block, and the + ve inserted SM are connected in series among these sections. Depending on the SMs' firing signals, several SMs are added to these sections. In contrast to the average model, in the switching model of the MMC, each SM is controllable and observable. The averaged model is based on model type 5 described in Cigre B4.57 [52], and it is simulated in the RTDS rack (core).

The upper and the lower-level controls of MMCs are based on the MPC proposed in [32] and the PI control published in Cigre B4.57 [52]. The details of PI control for different control loops are provided in Table 3. The MMC 1 is DC voltage controlled, while MMC 3 is active/reactive power controlled. Furthermore, MMC 2 and MMC 3 have direct voltage ($V_{ac} - f$) control. In this system, a decentralized controlling approach is considered.

Here, for the MPC will be used values for $a = 0.65$ and $N = 4$. For the cost function expressed by (8a), matrices $Q = 1 \times I$ and $R = 0.2 \times I$ are used, where I is an identity matrix. The prediction horizon (N_p) is set to 30 sampling instances. Further, all the physical quantities like current and voltages are normalized. In the simulations, the input amplitude and the input rate constraints are implemented in the inner and outer MPC for the entire prediction horizon. These constraints are given as

$$-0.04 \le v^{\Sigma}_{Mdqz} \le 0.04, \tag{15a}$$

$$-0.8 \le v^{\Delta}_{Mdqz} \le 0.8, \tag{15b}$$

$$-1 \le \Delta v^{\Sigma}_{Mdqz} \le 1, \tag{15c}$$

$$-1 \le \Delta v^{\Delta}_{Mdqz} \le 1. \tag{15d}$$

It should be noted that in RSCAD/RTDS, the response times of PI and MPC control are different. Fig. 5(a) depicts how the calculation times of the PI control evolve for different controlling loops. With the MPC, all control values are computed within the shortest control interval of 80 µs, as can be seen in Fig. 5(b).

3.2. Cable model

The cable is modeled by the traveling wave cable model routine. Among the two traveling wave cable models, the Frequency-Dependent Phase model is used. Due to its higher accuracy which is shown during controller interactions [53]. The cable data for XLPE submarine cables are used.

3.3. VARC DC CB model

The detailed model structure, operating principle, and experimental validation of the VARC DC CB have been discussed in [30,54–56]. The authors have used four 80 kV VARC modules for a 320 kV MTDC system. Thus, high computational power is required. Since one of this paper aims to understand the interaction between the advanced control and the VARC DC CB, some simplifications are made. The stray capacitance across the vacuum breaker and the surge arrester that exist in the VARC DC CB can be neglected. During some operation intervals, specific VARC DC CB modules branches are connected in series, and the model can be aggregated. As a result, a single representation is obtained as shown in Fig. 6.

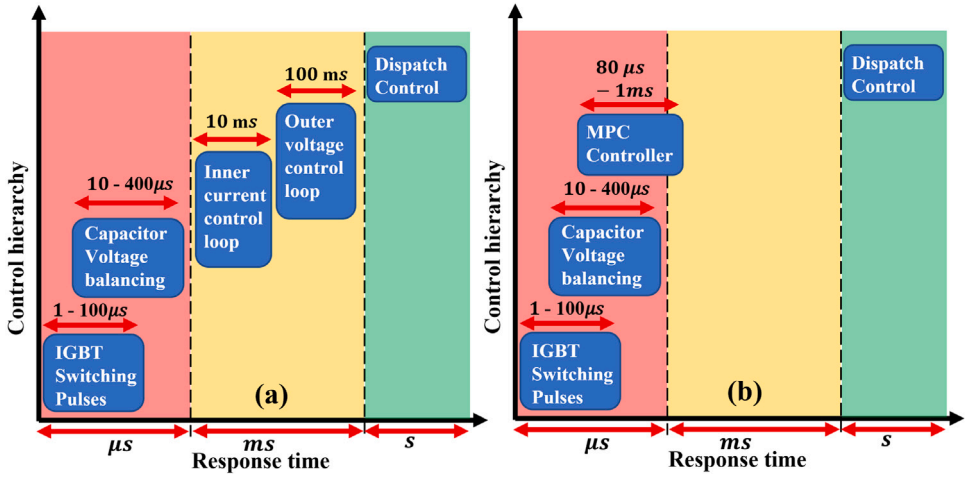

Fig. 5. Overview of the control hierarchy of MMC: (a) PI-based control hierarchy; (b) MPC-based control hierarchy.

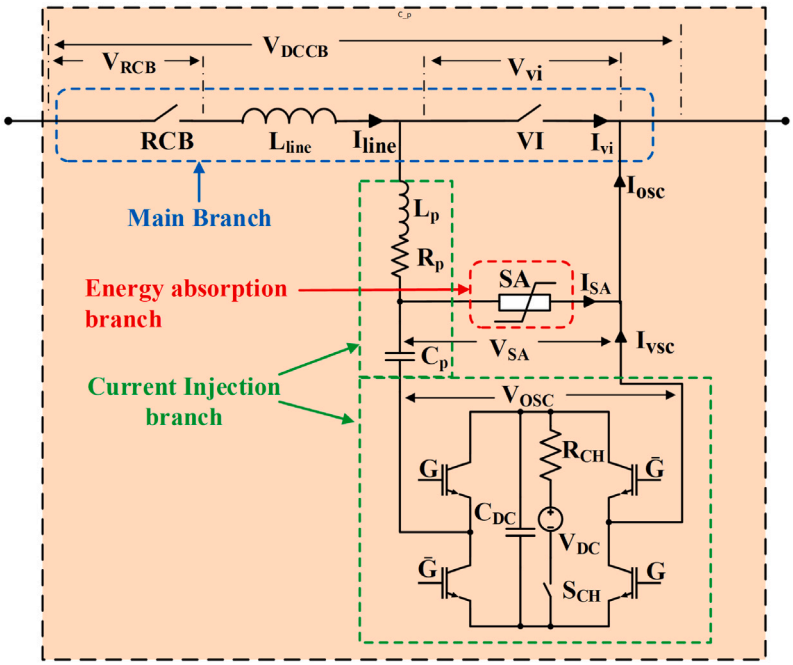

Parameter	Symbol	320 kV System	200 kV System
Oscillation Inductor	L_p	300 μH	$300 \times \frac{3}{4} = 225\ \mu H$
Oscillation Resistor	R_p	0.5 Ω	$0.5 \times \frac{3}{4} = 0.375\ \Omega$
Oscillation Capacitor	C_p	0.66 μH	$0.66 \times \frac{4}{3} = 0.88\ \mu F$
Rated/Clamping voltage of surge arrester	-	320 / 480 kV	200 / 300 kV
Initial Voltage across C_p	$V_{in\ C_p}$	24 kV	$24 \times \frac{3}{4} = 18\ kV$
Line inductor	L_{line}	80 mH	80 mH

Fig. 6. An illustration of a VARC DC CB with downscaled parameters for a 200 kV system.

3.4. Wind power plant model and controls

The wind power plant model consists of two major sections; a permanent magnet generator (PMSM)-based wind turbine and an interface transformer with a high pass filter. For a PMSM-based wind power plant, back-to-back VSCs are connected to the interface transformer at one AC end, and the PMSM at the other AC end. Both VSCs, i.e., the grid side converter (GSC) and the machine side converter (MSC), are Neutral point Clamped (NPC) three level type converters. The DC bus is represented by a small reactor. The neutral point of the GSC's capacitor is connected to the ground to block zero-sequence voltage and the 3rd harmonic component produced by PMSM. The d-component of the input current is used to maintain the capacitor voltage as a part of GSC control. The neutral point voltage balance is achieved by introducing a DC side voltage balance, where the small offset is calculated and added to PWM modulating waveforms in consecutive half-cycles [57].

The characteristic equations of the GSC at the PCC in a dq rotating frame are given as [58]:

$$v_{md}^G = v_d^G + R^G i_d^G + L_L^G \frac{\mathrm{d}i_d^G}{\mathrm{d}x} - \omega^G L_L^G i_q^G, \tag{16a}$$

$$v_{mq}^G = v_q^G + R^G i_q^G + L_L^G \frac{\mathrm{d}i_q^G}{\mathrm{d}x} + \omega^G L_L^G i_d^G, \tag{16b}$$

where $v_{md}^G = \frac{1}{2} m_d^G V_{dc}^{bus}$ and $v_{mq}^G = \frac{1}{2} m_q^G V_{dc}^{bus}$ are the dq components of the modulating voltages of GSC, being the product of the modulation index m and DC bus voltage V_{dc}^{bus}. Furthermore, R^G is the leakage resistance, L_L^G is the leakage inductance, i_d^G and i_q^G are the grid currents in dq-frame and ω^G is the angular grid frequency.

The PMSM is rated at 4 kV, 2 MW at wind speed of 12 m/s. An interior magnet machine with a sinusoidally distributed winding is considered during the modeling of PMSM. As Clark-Park transformation is used, PMSM is represented in a dq-frame as [58]:

$$v_{md}^P = R^P i_d^P + (L_{Md}^P + L_L^P) \frac{\mathrm{d}i_d^P}{\mathrm{d}x} - \omega_r^P (L_{Md}^P + L_L^P) i_q^P, \tag{17a}$$

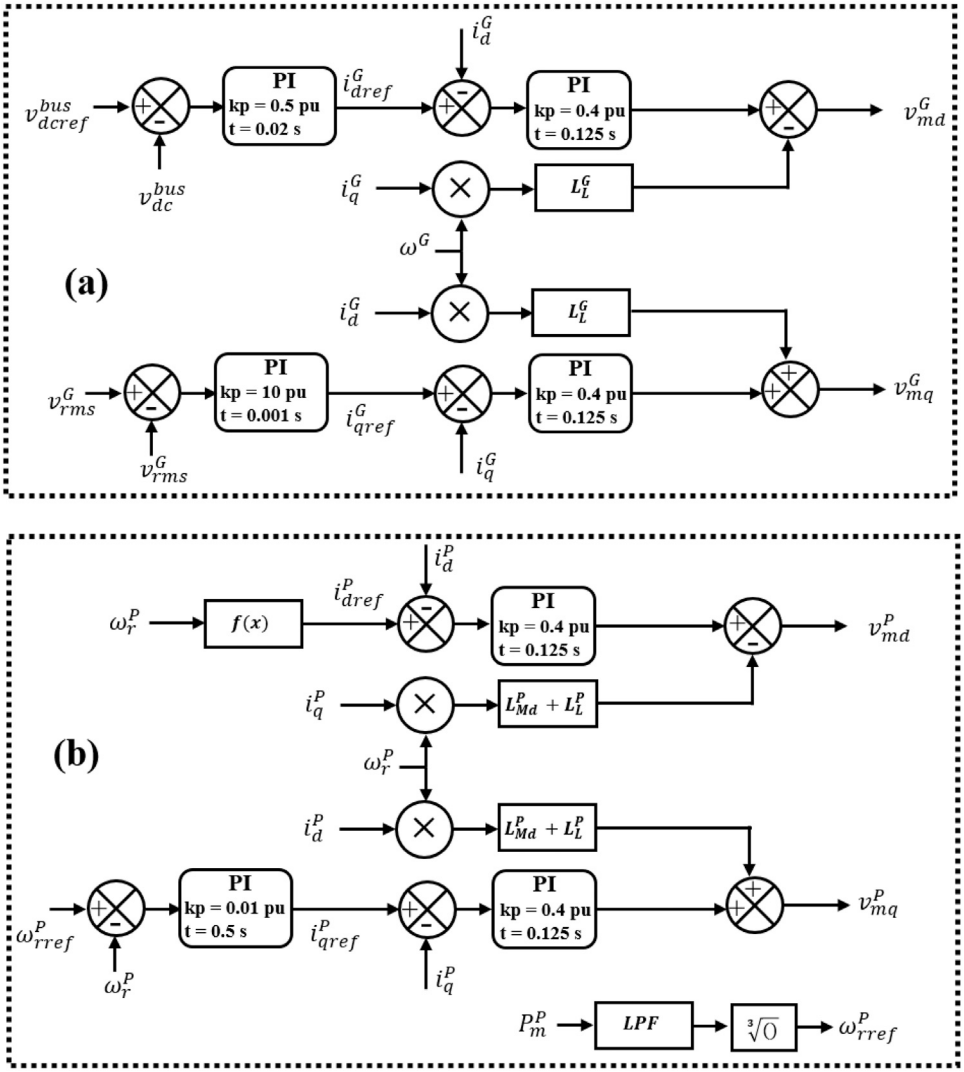

Fig. 7. Controller scheme for: (a) grid side converter (GSC); (b) machine side converter (MSC).

$$v_{mq}^P = R^P i_q^P + (L_{Mq}^P + L_L^P)\frac{\mathrm{d}i_q^P}{\mathrm{d}x} + \omega_r^P(L_{Mq}^P + L_L^P)i_d^P + \omega_r^P \Psi_f^P, \tag{17b}$$

$$T_e^P = \frac{3}{2}\left[\hat{\psi_f^P} i_q^P + (L_{Md}^P - L_{Mq}^P) i_d^P i_q^P\right], \tag{17c}$$

where $v_{md}^P = \frac{1}{2} m_d^P V_{dc}^{bus}$ and $v_{mq}^P = \frac{1}{2} m_q^P V_{dc}^{bus}$ are the dq components of the modulating voltages of PMSM, as a product of the modulation index m and the DC bus voltage V_{dc}^{bus}, R^P is the stator resistance, L_{Md}^P and L_{Mq}^P are the mutual inductances in the dq-frame, L_L^P is the stator leakage inductance, i_d^P and i_q^P are the stator current in dq-frame, ω_r^P is the rotor electrical speed, T_e^P is the developed toque by PMSM and Ψ_f^P is the permanent magnet flux. The model of the wind turbine is derived considering steady-state wind power:

$$P_m^P = c_p(\lambda, \beta)\frac{\rho A}{2} v_{wind}^3, \tag{18}$$

where P_m^P is the mechanical power output of the turbine, ρ is the air density, A is the area swept pot by the turbine blade, v_{wind} is the wind velocity, and $c_p(\lambda, \beta)$ is the performance coefficient of the turbine, which is a function of tip speed ratio λ and the blade pitch angle β.

A classical PI controls control the offshore wind farms. The GSC controls the active and the reactive power exchange between the wind power plant and the offshore AC grid. The dq current decoupling method is used as shown in Fig. 7(a). The active power reference is computed in a way that the DC bus voltage is maintained at a constant value, whereas the reactive reference is computed to support the offshore AC voltage.

For a higher PMSM efficiency, MSC controls maintain the 180-degree phase shift between the stator current and voltage. The quadrature axis component of the stator current maintains the power requested by the wind turbine as shown in Fig. 7(b). The rotor speed is a cubic function of power, while the direct component of the stator current controls the reactive power at its minimum level until the rated power is reached. This is carried out by storing the d-axis stator current in a table (formatted as $y = f(x)$), where the output is the function of the rotor electrical speed.

The interface transformer performs two functions. Firstly, it connects the large time step (i.e., 80 μs) network to the small-time step network. Secondly, it is used to represent an entire wind farm. The scaling increases the MVA power and current ratings. The PWM scheme is used, where switching occurs at 19 times the fundamental frequency. Therefore, the current and the voltage harmonics appear to be around the switching frequency. For this reason, a high-pass filter is implemented at the large time step network side of the interface transformer.

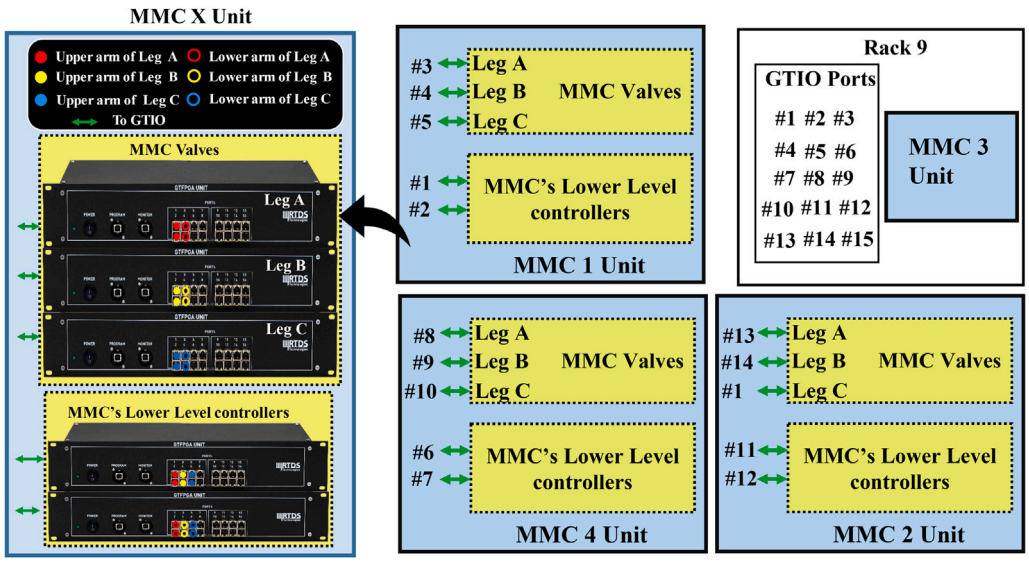

Fig. 8. Overview of the GTIO port connections between GTFPGA and RTDS.

4. Simulation tool configuration

4.1. NovaCor rack and GTFPGA configuration

In RTDS/RSCAD, on one GTFPGA can be programmed two MMCs, namely, *'rtds_vsc_FPGA_U5'* and *'rtds_vsc_FPGA_GM'* models [59]. The later MMC model can simulate IGBT faults within the SM(s). However, it comes with an extra computation burden, and as a result, one GTFPGA unit can be used to simulate one leg. Hence, to represent an MMC unit, three GTFPGA units are required. The GTFPGA unit is connected to the GTIO port of RTDS via a full-duplex optical fiber using the Aurora protocol [59]. The *'rtds_vsc_FPGA_GM'* model uses 2 additional GTFPGA units for capacitor voltage balancing of MMC's sub-modules known as "MMC's lower level controller". Each leg sends SM capacitor voltage values and receives Firing sequence over two full-duplex optical fibers from MMC's lower level controller, as shown in Fig. 8. Using this configuration, 5 GTFPGA units are used to represent one MMC.

Due to a large number of system nodes, the meshed HVDC system is programmed on one RTDS rack. The MPC is programmed on another rack, as shown in Fig. 4. Hence, this rack can be considered an external cubical control. The cross-rack communication is performed by a global bus hub and an IRC switch.

4.2. Software-in-the-loop setup

A wind gust data expressed in meter per second (m/s) measured near the Orkney Islands (58.9809° N, 2.9605° W) and Shetland Islands (60.5297° N, 1.2659° W) are adopted from [60], which represents the OWF 1 and OWF 2 wind profiles, respectively. A *Selenium* tool is used to extract the wind speeds from the web using Python. These wind data are communicated through a TCP/IP connection to RSCAD with a communication delay of 100 ms, and the update rate is every 2 s. An illustrated overview of the software-in-the-loop is shown in Fig. 9.

5. Simulation results

Considering the full selective HVDC protection scheme, the blocking of all MMCs is disabled. Furthermore, the internal protection of the MMCs is disabled to test the performance of both controllers under the worst operating conditions. In all cases, the disturbance (small and large) takes place at $t = 0.2$ s. In the mentioned case studies, the circulating current suppression control (CCSC) is enabled for all the converters. During the steady-state conditions prior to AC and DC fault occurrence, Fig. 10 shows the CCSC for MMC 2 with a PI and MPC control in the abc and dqz rotating frames. Next, CCSC is enabled at 0.1 s. Likewise, Fig. 11 shows the first and the last four upper and lower SM capacitor voltages for phase C of MMC 2 during the steady-state condition before AC or DC faults take place.

The following case studies are performed to identify the dynamic performance of the control and protection along with its effect on the system. For each case, the PI and MPC controlled MMCs' performances are compared.

5.1. Transients during nominal operation

To evaluate the controller's performance, an increase of the wind power (case 11), active power injection into the weak grid (case 12), and a re-close of cable 12 (case 13) are conducted in this study.

For case 11, Fig. 12 shows the performance of the MPC and PI controlled MMC during the higher wind gust of OWF 1 and OWF 2. Before the disturbance, OWF 1 and OWF 2 transfer active power of 202 MW and 221 MW, respectively, into the HVDC grid through MMCs 2 and 4. MMC 3 absorbs 400 MW from the HVDC grid. The surplus power within the DC grid is injected into a strong AC grid to maintain the DC voltage. At 0.2 s, an extra 201 MW and 218 MW are injected by OWF 1 and OWF 2, respectively. With the same active power by MMC 3, the DC voltage increases to a new steady-state value at the MMCs' terminals, except the one near MMC 1 (due to DC voltage control), as shown in Fig. 12(a). However, during the transient period, the MPC-controlled DC grid regulates the DC voltage at the rated value with an overshoot of 0.1% and a short settling time of 0.3 s (for 0.125% of the steady-state value), as shown in Fig. 12(a). Likewise, an overshoot of 0.825% in the DC voltage is observed for the PI-controlled MMC with a settling time of 1.48 s (for 0.125% of steady-state value). Furthermore, MPC-controlled MMC provides a higher damping in the offshore and the onshore AC voltage grids, as seen in Fig. 12(c).

Case 12 demonstrates an active power injection into the weak grid, and it is depicted in Fig. 13. It shows the capability of active power regulation. Initially, no active power is injected into the weak grid, as seen in Fig. 13(b). Then, OWF 1 and OWF 2 provide an active power of 304.4 MW and 330.4 MW into the HVDC grid. To keep the DC voltage fixed to the rated value, more power is injected into the AC grid through MMC 1, which behaves as a slack bus. At 0.2 s, 400 MW of power is injected into a weak grid keeping the AC terminal voltage stable with MMC 2's AC voltage support. The active power injection into the weak

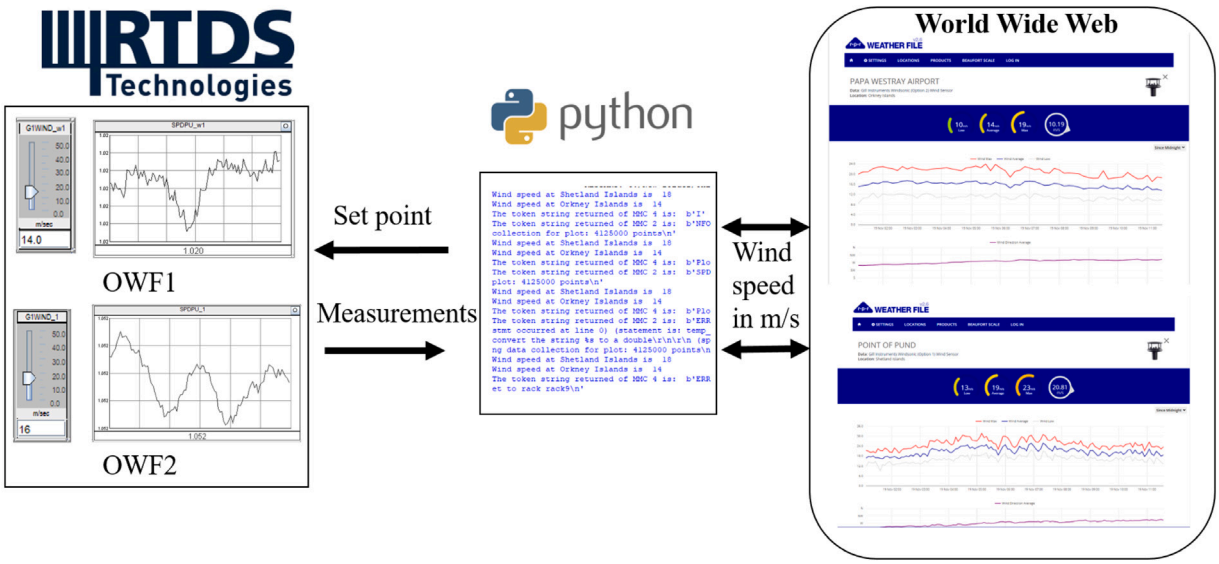

Fig. 9. Overview of software-in-the-loop setup.

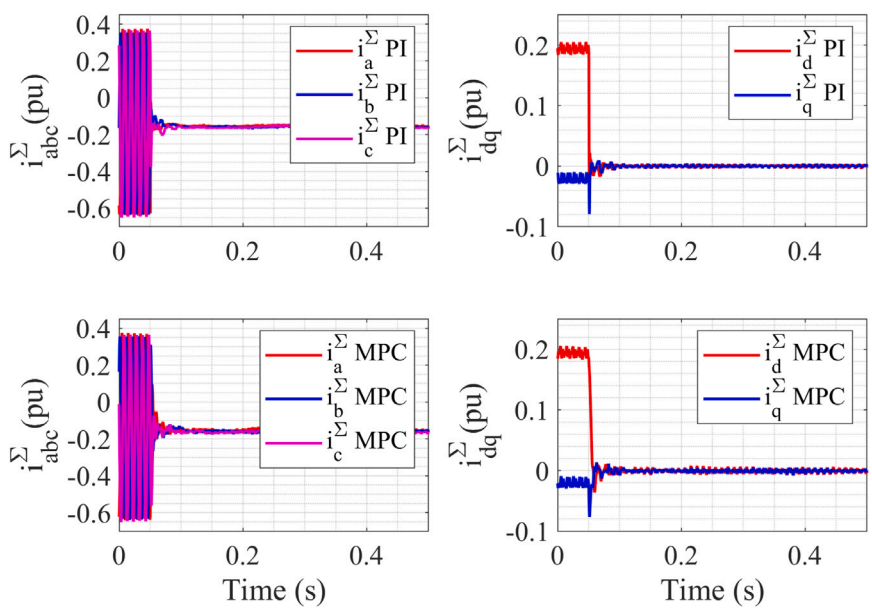

Fig. 10. Circulating current suppression control in MMC 2 with a PI and a MPC control.

grid creates a power shortage in the HVDC grid, and the DC voltage drops, as seen in Fig. 13(b). The DC voltage drop for the MPC-controlled MMCs near MMC 2 is 101 V/ms, while for the PI-controlled MMCs is 78 V/ms. The high voltage drop in the case when MPC is used occurs due to the faster response of the MPC at MMC 2. However, with the fast power support from MMC 1, the DC voltage decreases to 396.1 kV, as seen in Fig. 13(a) and settles to 398.6 kV. In the case of a PI-controlled DC grid, the DC voltage reaches the negative peak of 393.5 kV. A fast control action of the MPC influences slow transient oscillations. The DC voltage swing is within ± 2 kV around the steady-state value with the frequency of 9 Hz and a damping of 0.1 kV per cycle. Furthermore, it is observed that this slower oscillation is reflected in the state variables of the DC and AC grids, which induces slow transient oscillations of 9 Hz and 12 Hz in offshore and onshore AC grids. The time taken by the MPC to reach the active power reference in MMC 3 is 120 ms, while the PI controller takes 260 ms, as shown in Fig. 13(b).

Fig. 14 indicates the controllers' effect and performance with the reclosing of the DC CB and putting cable 12 in service. During the pre-disturbance stage, the active power from OFW 1 is transferred to the onshore grids through four other DC cables. The DC bus voltages near MMCs 1 and 2 are 400 kV and 408 kV, respectively (see Fig. 14(a)). Upon re-close of cable 12 from both ends at 0.2 s, there is a current surge in the cable with the peak value of 2.73 kA, which oscillates at 112 Hz as observed in Fig. 14(c). This oscillation is caused by the charging of the cable's capacitance and the interaction with the line inductance of the DC CB, which is given by equation $\frac{1}{\sqrt{LC}}$, where $L = 80$ mH and $C = 0.125\,\mu$F/km. However, this oscillation is damped around the steady-state value at the time instant of 0.44 s for the MPC-controlled DC grid, while PI takes 0.5 s to settle. Due to the restoration of cable 12, the DC bus voltage at MMC 2 decreases to a new steady-state value. The current surge in the cable produces a larger MMC 1's arm current (as shown in Fig. 15) and MMC 2's arm current, which in a realistic system leads to converter blocking. Furthermore, this surge has a minimum impact on MMCs 3 and 4, and the AC grids they are connected to, as they are not directly connected to cable 12. These current surge suppression can be done by introducing a high value of inductance in series with cable 12. Addition of this inductance not

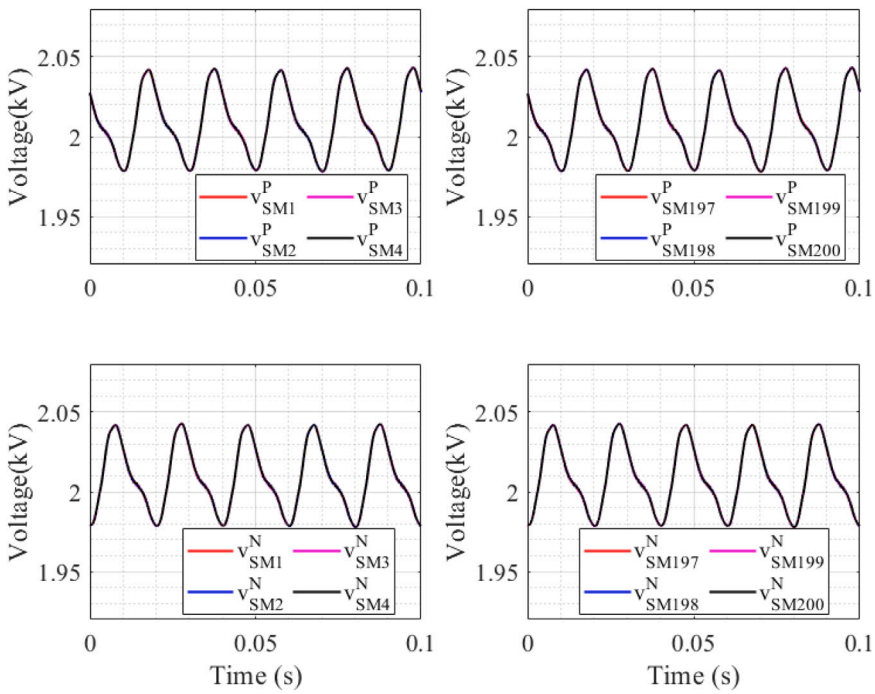

Fig. 11. The first and the last four upper and lower SM capacitor voltages for the phase C of MMC 2.

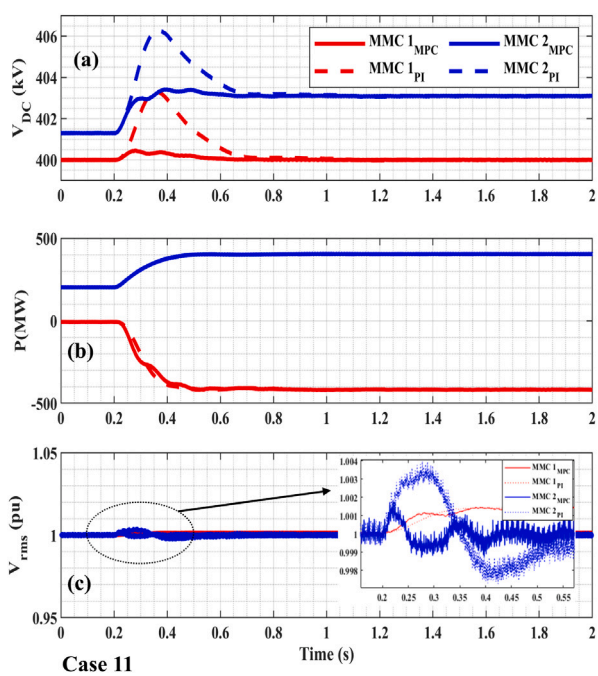

Fig. 12. Case 11: (a) MMC's voltage [kV], (b) active power [MW], and (c) RMS AC voltages [pu].

only suppress this surge but will aid in current interruption. However, high value of inductance will have negative impact on the converter's control. Thus a appropriate a value of inductance need to be selected. However, the possibility of suppressing this current by control action is out of scope of this paper and will be investigated in future work.

5.2. AC grid side fault analysis

The two standard studies, i.e., symmetrical and asymmetrical fault cases, are simulated at two different locations: at the PCC of MMC 1 and at the PCC of MMC 2. As a result, three cases are considered: a three-phase fault at PCC of MMC 1 (case 21), a phase-to-ground fault at PCC of MMC 1 (Case 22), and a three-phase fault at PCC of MMC 2 (Case 23). The pre-fault condition is shown in Fig. 16.

Fig. 17 depicts the performance of the MPC and the PI-controlled MMCs during the three-phase fault at the PCC of MMC 1. This fault is self-clearing, and the duration is 200 ms. The terminal AC voltage collapses during the fault at PCC of MMC 1, as seen in Fig. 17(c). Since MMC 1 controls the DC grid voltage, after an AC fault takes place, MMC 1 losses its synchronization. Due to the fault, the power delivered by the MMC 1 goes to zero. With the same power infeed from the OWFs and the power extraction by MMC 3, the DC grid voltage increases to 468

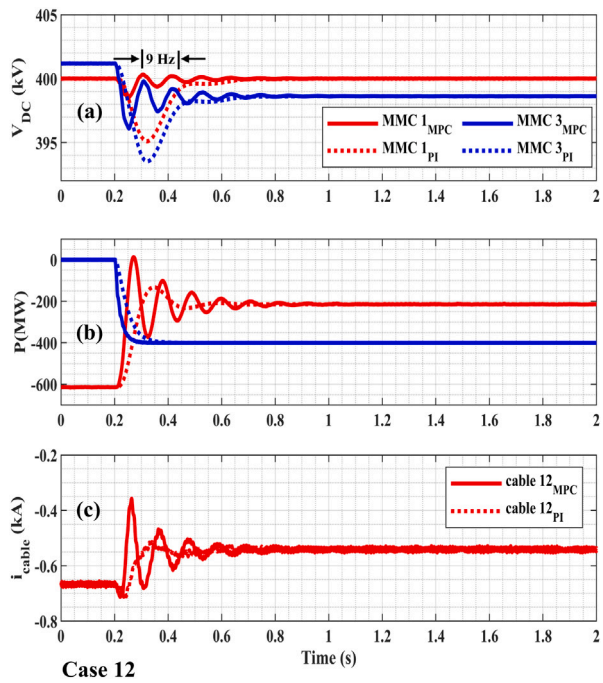

Fig. 13. Case 12: (a) MMC's voltage [kV], (b) active power [MW], and (c) current of the positive part of cable 12 [kA].

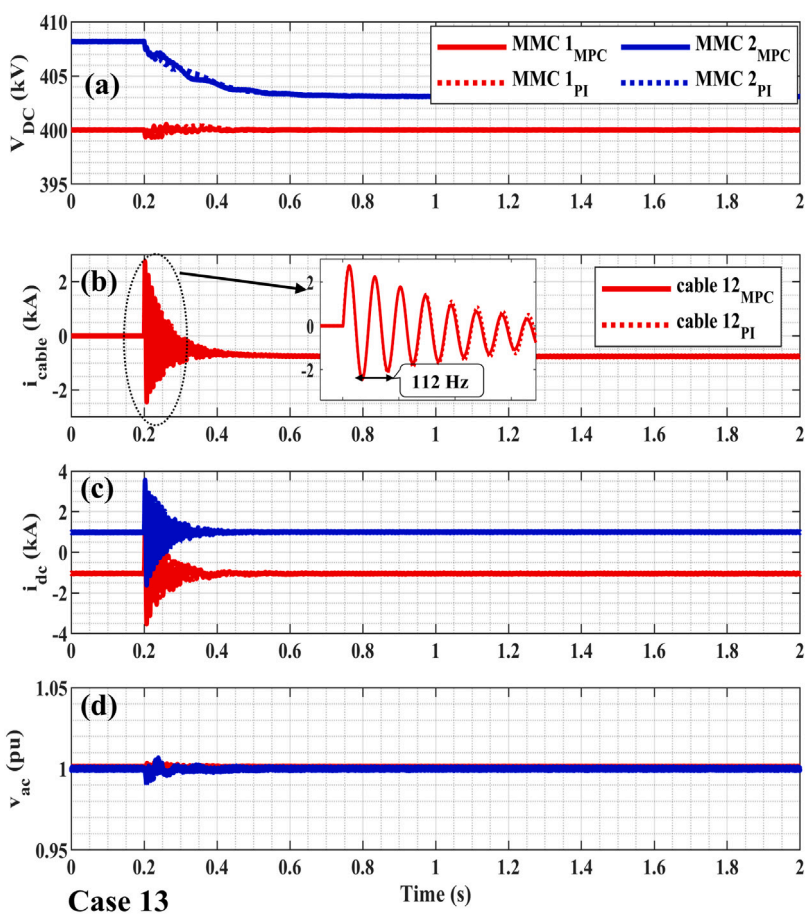

Fig. 14. Case 13: (a) MMC's voltage [kV], (b) current of the positive part of cable 12 [kA]; (c) positive MMCs' currents [kA], and (d) RMS AC voltages [pu].

kV, as seen in Fig. 17(a). During the fault, offshore AC grid voltage, in the case of the PI-controlled DC grid, produces an over-voltage of 3%, which is absent in the MPC-controlled DC grid (indicated in Fig. 17(c)). Furthermore, the AC side fault near MMC 1 causes a large arm current, as seen in Fig. 20. For both controllers, the arm current increases during the fault. However, the MPC restricts this rise to a lower level. This

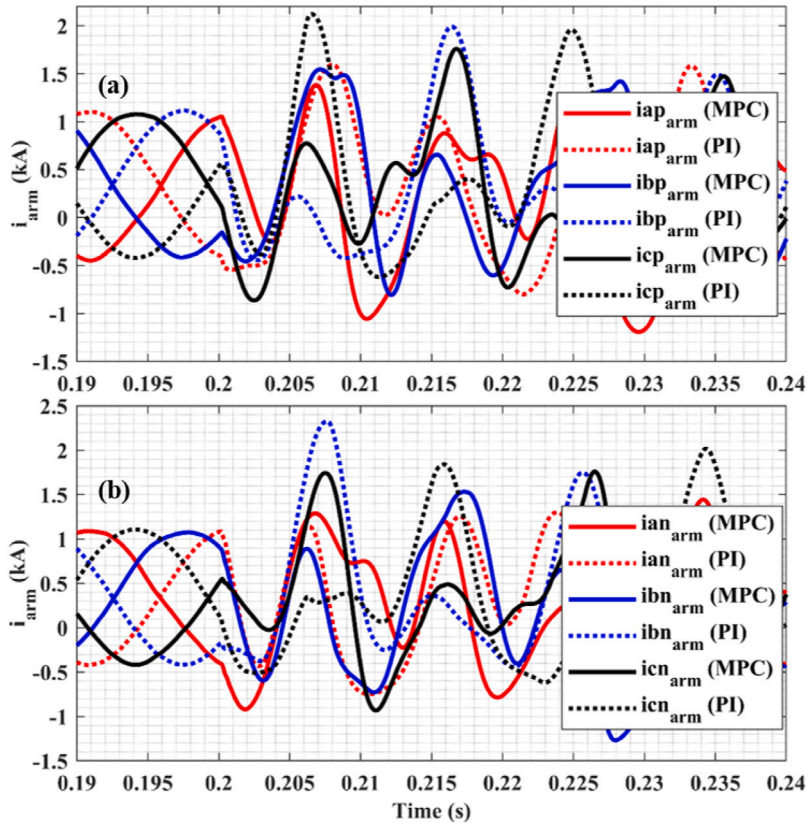

Fig. 15. Three-phase MMC 1's arm currents in: (a) upper arm; and (b) lower arm during re-closing of cable 12.

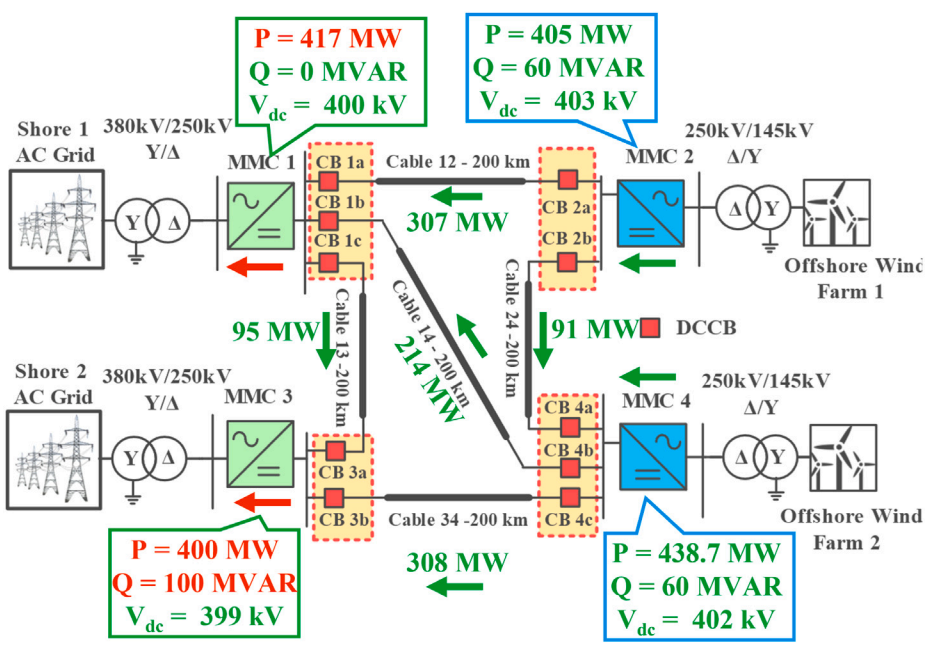

Fig. 16. Steady-state condition before AC and DC fault.

restriction is enabled with the MPC constraints in MMC 1. However, the MPC takes longer time to recover after the fault is cleared due to the input constraints. As a result an DC over-voltage 486 kV near MMC 1 with a higher settling time as compared to PI controller. Still, the MPC at MMC 1 regulates the arm current and power, as seen in Figs. 17(b) and 17(d). Further, the performance of MPC can be enhance by introducing the drop based control strategies at the PQ controlled converter.

Fig. 18 shows the impact of a temporary single phase-to-ground at PCC of MMC 1 considering PI and MPC controllers. With a phase-to-ground fault at PCC of MMC 1, the AC voltage at PCC drops. However, there is an oscillation of 100 Hz at the PCC during a fault. This

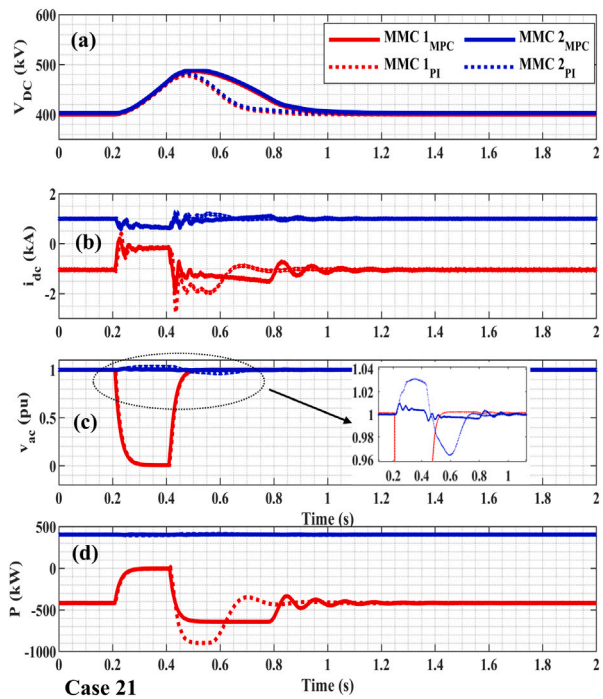

Fig. 17. Case 21: (a) MMC's voltage [kV], (b) positive MMC's current [kA], (c) RMS AC voltages [pu], and (d) active power [MW].

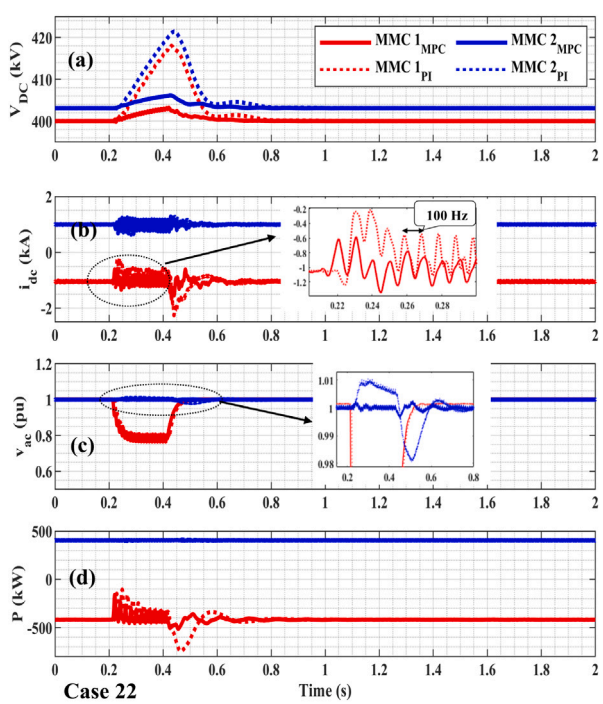

Fig. 18. Case 22: (a) MMC's voltage [kV], (b) positive MMC's current [kA], (c) RMS AC voltages [pu], and (d) active power [MW].

onshore oscillation propagates into the DC grid as seen in Fig. 17(a). Furthermore, it is also reflected in the offshore AC grid but with a lower amplitude. During the fault, the DC overvoltage observed with MPC-controlled is 0.5%, while with PI-controlled converter is 4%. Comparing both controllers, MPC provides better performance during the fault and post-fault period in terms of response and stability. In case of a phase-to-ground fault at the PCC of MMC 1, at $t = 0.2$ s, the AC voltage at PCC drops to 0.78 p.u for both controllers as seen in Fig. 17(c). During the fault, the arm current of PI-controlled MMC 1 has a peak value of 2.8 kA, whereas the arm current of the MPC-controlled MMC 1 has the peak of 1.8 kA, as depicted in Fig. 21.

Fig. 19 depicts the performance of the MPC and the PI controlled MMCs during the temporary three-phase fault at the PCC of MMC 2. During the three-phase fault, the AC voltage at MMC 2's PCC decreases to zero, as observed in Fig. 19(c). The fault creates a power shortage of 405 MW. MMC 1 injects the required power into the DC grid to maintain the rated DC voltage, which is indicated by the power reversal in Fig. 19(d). It is observed that the MPC-controlled MMC 1 regulates the DC grid voltage quickly, with a DC voltage drop of 3% at MMC 2 and 2% at the MMC 1 terminal. However, in the PI-control case, the DC grid experiences a DC voltage drop of 7.4% at MMC 2 and 5.75% at MMC 1. Furthermore, the higher voltage drop generates a significant overshoot of 30% at the PCC of MMC 4. Due to the fast control of the MPC over the DC voltage and the offshore AC voltage, the overshoot is 7%. The MPC-controlled DC grid shows a faster recovery than the PI-controlled DC grid, as seen in Fig. 19.

5.3. DC grid side fault analysis

The steady-state solution (i.e., power flow solution) of the four-terminal HVDC system is depicted in Fig. 16. For the DC fault analysis, a pole-to-pole fault on cable 12 near MMC 1 (case 31), a pole-to-pole fault on cable 34 near MMC 3 (case 32), and eight MMC 1 sub-module faults (case 33) are performed.

During the pole-to-pole fault near MMC 1 on cable 12 at 0.2 s, the DC voltage of MMC 1 drops until the DC CB operates. With the higher potential provided by the surge arrester of the DC CB, the fault current in cable 12 reaches a peak value of 7.2 kA (as shown in Fig. 22(d)). Due to the fast recovery of the MPC-controlled DC grid, the DC voltage drops near MMC 1 and is restricted to 397 kV, as seen in Fig. 22(a), while in PI-controlled MMC 1, the DC voltage decreases to 395 kV. After the fault is cleared, the MPC provides higher damping, resulting in faster post-fault recovery. When cable 12 is disconnected, power redistribution occurs. This redistribution is due to potential differences at the MMC terminals. MMCs 2 and 4 are the grid forming offshore converters, which reduce the impact on the onshore AC grids during and after the fault.

With a pole-to-pole fault near MMC 3 at cable 34, the DC voltage near MMC 3 decreases to 388 kV. The recovery of the MPC-controlled MMCs DC grid is faster with the decreasing rate of 273.33 V/ms, whilst for a PI-controlled MMCs DC grid's decreasing rate is 135.34 V/ms as seen in Fig. 23(a). The VARC DC CB receives the trip signal after 3 ms, and the maximum fault current rises to 7 kA (as seen in Fig. 23(d)). Since the MMC 2 is connected to a weak grid, there is a damped oscillation of 125 Hz after the fault is cleared, as seen in Fig. 23(c). However, when the AC voltage is controlled, this oscillation is damped.

In the case of eight internal SM faults in the upper and lower leg of phase A of MMC 1, a lower order frequency oscillation is observed in the AC and DC voltages of MMC 1. For PI-controlled MMCs, the oscillation frequency is 100 Hz, while for the MPC-controlled MMCs, the oscillation frequency is 59 Hz. The oscillation of the DC voltage observed at the MMC 1's terminal with an MPC control has a peak-to-peak value of 0.6 kV from the pre-disturbance value. However, using the PI control, the peak-to-peak value is 0.2 kV. Moreover, this oscillation is restricted to the MMC 1's AC and DC terminals only, as seen in Figs. 24(a) and 24(b).

5.4. Control interoperability

To understand the controller interaction, the following case studies are performed for MMC 1, as they are graphically illustrated in Fig. 25:

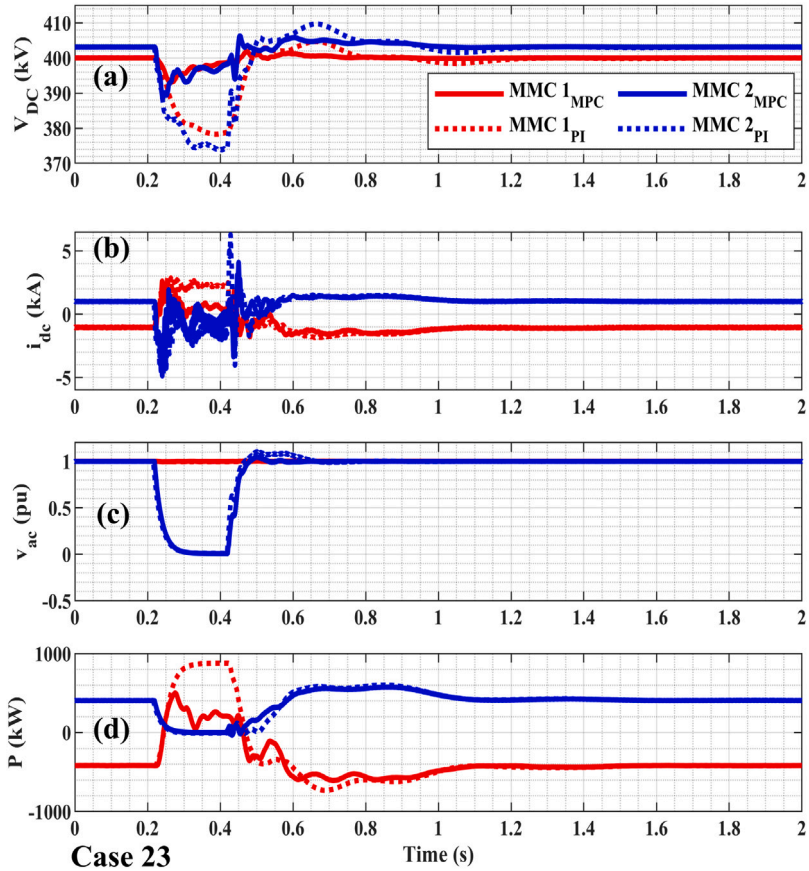

Fig. 19. Case 23: (a) MMC's voltage [kV], (b) positive MMC's current [kA], (b) RMS AC voltages [pu], and (d) active power [MW].

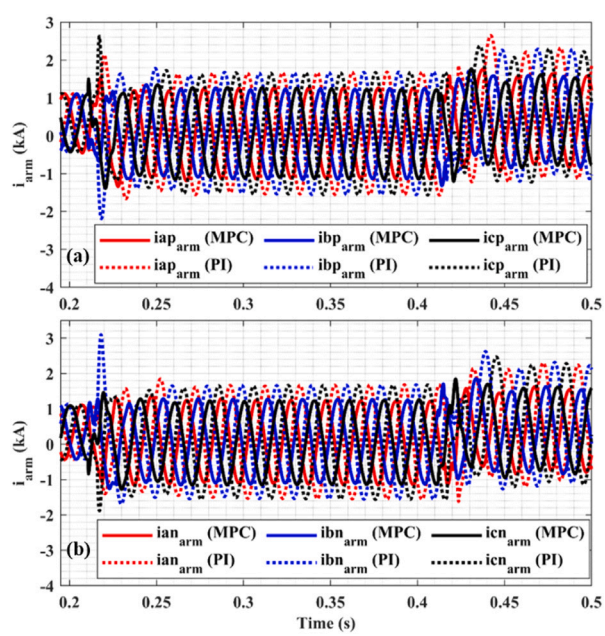

Fig. 20. Three-phase MMC 1's arm currents in: (a) upper arm; and (b) lower arm during three-phase fault.

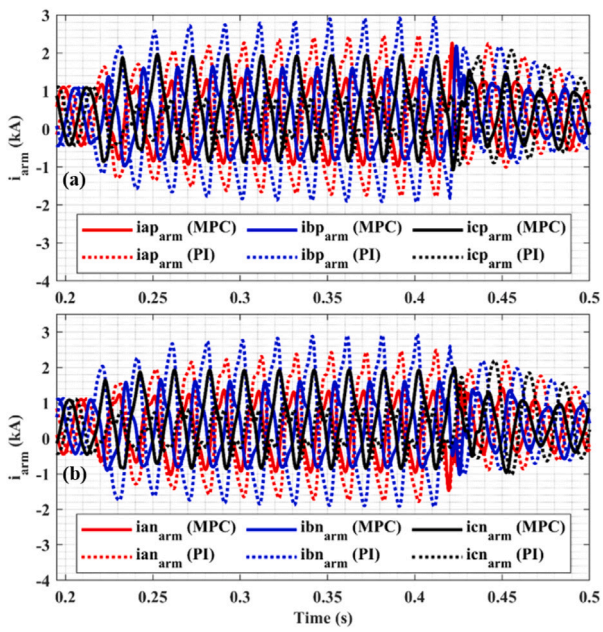

Fig. 21. Three-phase MMC 1 arm currents in: (a) upper arm; and (b) lower arm during single-phase fault at PCC of MMC 1.

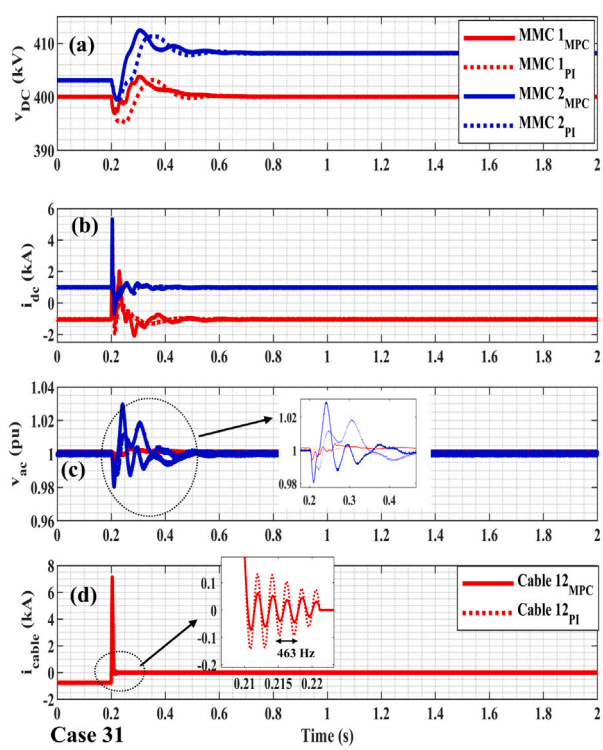

Fig. 22. Case 31: (a) MMC's voltage [kV], (b) positive MMC's current [kA], (c) RMS AC voltages [pu], and (d) positive cable 12 current [kA].

- Case 1 - all PI controllers — In this case, the inner current, the outer voltage, and the circulating current suppression controls of MMC 1 are realized using classical PI controllers. The proportion gains and the integral time constants for different loops are summarized in Table 3 and taken from [52].

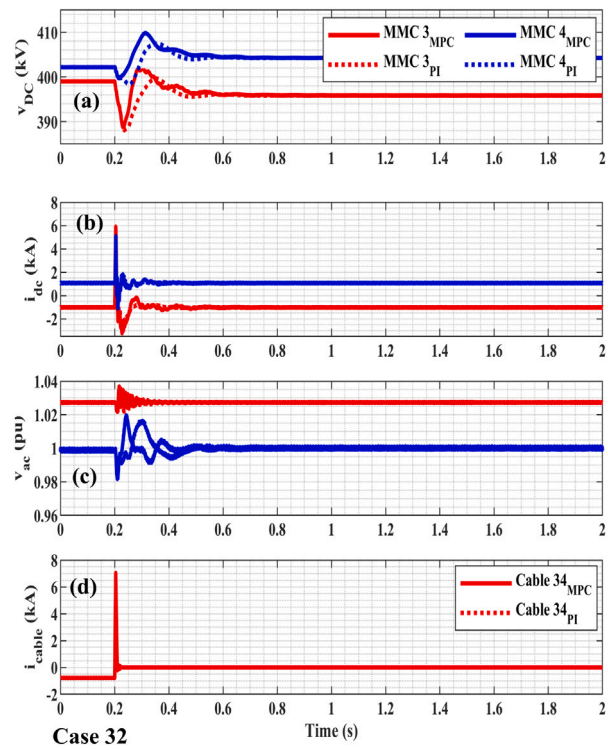

Fig. 23. Case 32: (a) MMC's voltage [kV], (b) MMC's current [kA], (c) RMS AC voltages [pu], and (d) positive cable 34 current [kA].

- Case 2 - PI controller in cascade with the inner MPC controller — In this case, the DC voltage control of MMC 1 is realized as a PI controller. The output of this controller provides the reference to the MPC controller.
- Case 3 - all MPC controllers — In this case, all control loops of MMC 1 are designed using the MPC.

For this operating scenario, the system is analyzed before and after the change of the wind power. Before the disturbance, the wind farm near MMC 2 provides an active power of 10 MW. Similarly, the active power of 100 MW is produced by the wind farm near MMC 3. At $t = 0.5$ s, there is a sudden rise in the wind power with a time constant of 5 ms near MMC 2. Thus, the active power rises from 10 MW to 500 MW. A different controller combination shows a different reaction to this sudden change, as it is shown in Fig. 26. In the case of a classical PI controller (case 1), this rise in power stimulates the increase of the DC link voltages (Fig. 26(a)). The maximum percentage rise of the DC bus voltage varies with the bus location. Due to the DC voltage control at MMC 1, this voltage rise is restricted to 6%, whereas the DC link voltage at MMC 2 and MMC 3 rises by 7.82% and 8%, respectively. Furthermore, the converging time to the new steady-state is 1 s. For case 2, even with the presence of the MPC, a similar pattern is observed during the wind power increase at MMC 2. However, due to the MPC-based DC voltage controller in case 3, the maximum DC voltages rise of MMC 2 and MMC 3 is less than 4%, which is less than the standard DC voltage margin [61]. Also, the settling time of the DC-link voltage is 100 ms.

The active power injected into MMCs, and the cable currents are shown in Figs. 26(b) and (c), respectively. Compared to other cases, case 3 yields a faster and more stable response. Furthermore, the interaction with other MMCs' controllers can be seen in Fig. 27. The fast control action in case 3, provides a good reference for the PI controllers of MMC 2 and MMC 3 to achieve a new steady-state with a minimum deviation.

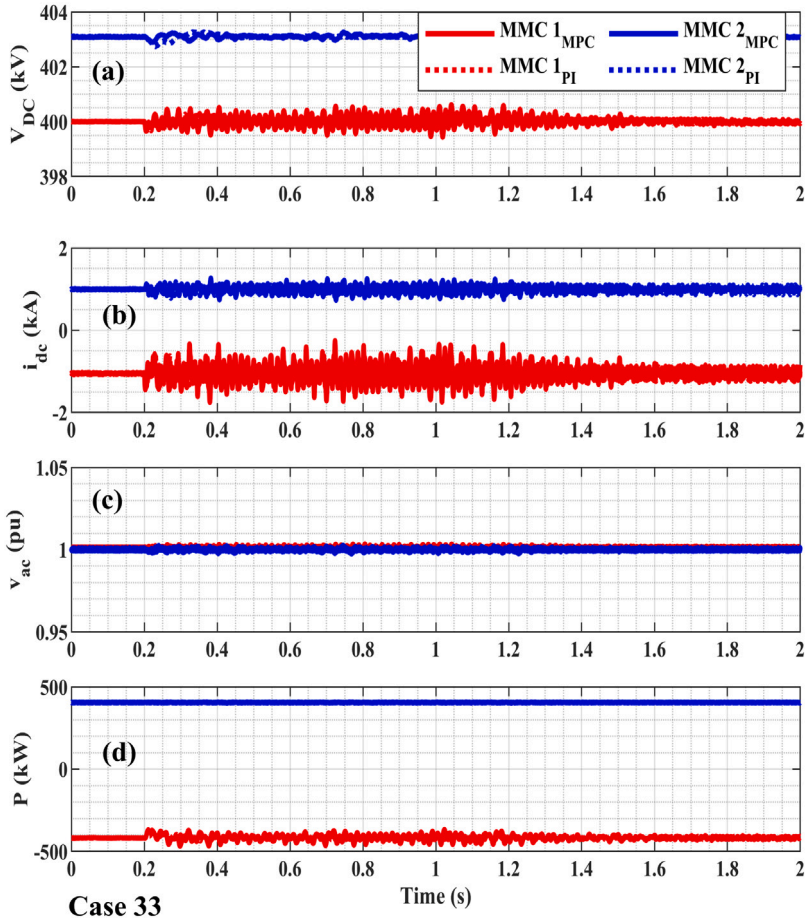

Fig. 24. Case 33: (a) MMC's voltage [kV], (b) MMC's current [kA], (c) RMS AC voltages [pu], and (d) active power [MW].

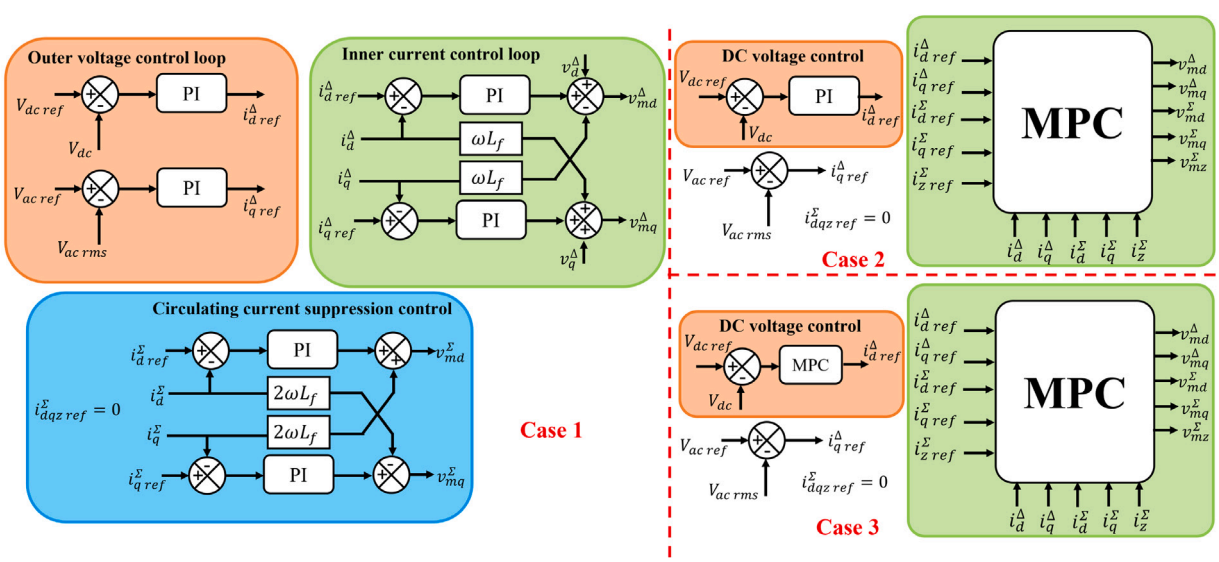

Fig. 25. Graphical representation of different cases implemented in MMC 1 control for interoperability studies.

The dynamic change of power causes an increase of the DC voltage for a few seconds in the case when a classical PI controller is applied(case 1). This sudden and longer duration of the DC overvoltage can create protection anomalies. Also, the effect of this overvoltage is propagated in the offshore grids. In this case, the fast control action will play a crucial role, leading to a optimal coordination between the advance control and protection. In this scenario, the combination of the advanced and classical controllers does not improve the performance

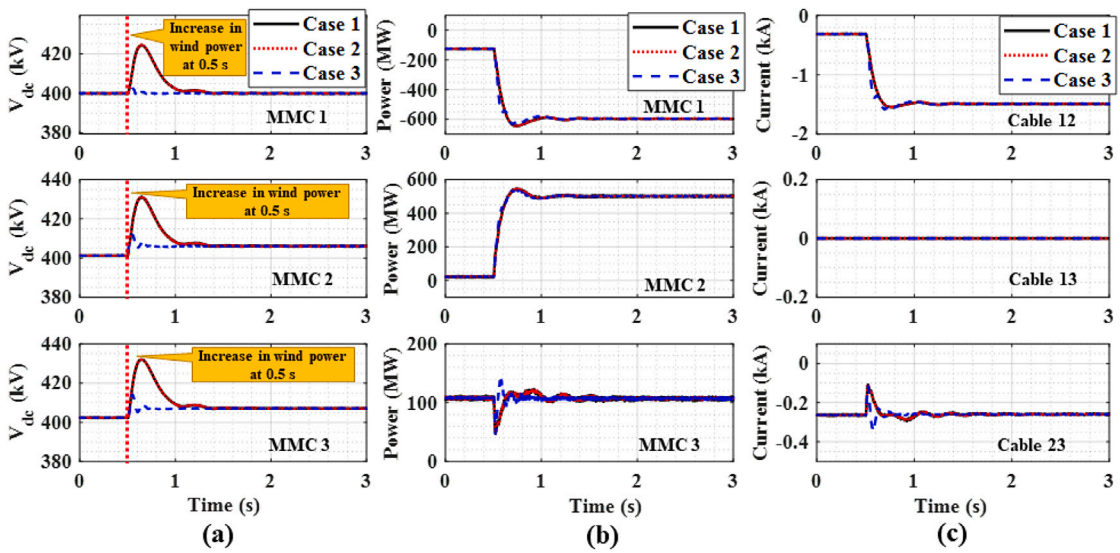

Fig. 26. Effect of the increase in the wind power (speed): (a) bus voltages of the MMCs; (b) active power at PCC of MMCs; (c) DC cable current.

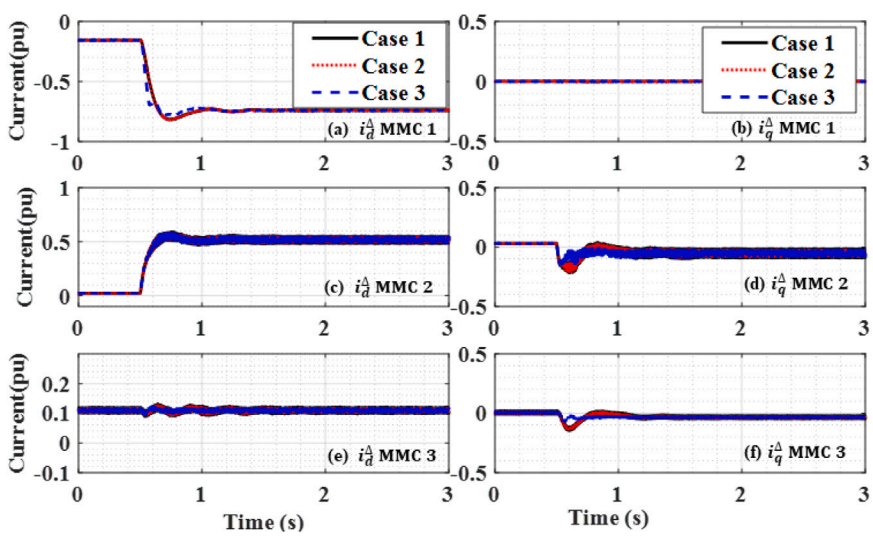

Fig. 27. Effect of the increase in the wind power (speed) on i_d^{Δ} and i_q^{Δ} grid current of MMCs.

compared to case 1. This poor performance arises due to the slower DC voltage control. Thus, re-tuning of the PI is required. In the future, faster power control will be needed to connect intermittent energy sources. Adaptive tuning of the PI or controllers like the MPC will be required at the converter's and system operator's levels.

6. Conclusion

This paper investigates the performance of the MPC in a four-terminal, monopolar, MMC-based HVDC grid connecting two offshore wind power plants, a weak grid and a strong grid, under fast transient like AC, DC faults and submodule internal faults. The paper also highlights the expansion of the control scheme from a single MMC terminal to a multi-terminal, indicating the MPC control's minimum tuning. The paper highlights the use of a switching model of an MMC by applying a GTFPGA in a hardware-in-the-loop and its interaction with average MMC model. Furthermore, SiL is used for an online update of the wind profile. The studies are conducted using RSCAD/RTDS simulations. The performance of the MPC is investigated against the traditional PI control.

The performance results show:

- The MPC-controlled MMC-based HVDC grid enables the converter to provide faster and more reliable controlled power support during the nominal operation with the minimum effect on the AC and DC terminal voltages than the PI-controlled MMC-based HVDC grid.
- The lower arm current and DC voltage droops are observed with the MPC-controlled MMCs during AC-side disturbances. Furthermore, the MPC-controlled MMC's post-recovery is faster than the PI-controlled ones.
- During DC fault, the MPC provides rigid terminal DC voltage support with a fast and damped recovery.
- The propagation of AC and DC side disturbances (faults) is smaller when the control is a MPC than PI-controlled MMCs. Furthermore, the MPC-based grid forming converter provides good voltage stability compared to the one with a PI control. During the interoperability studies, the slower response of the PI controller creates a bottleneck in the system recovery. Thus, the parameter of the PI controller needs to be re-calibrated. In contrast, the MPC provides a faster and more stable response.

Nevertheless, both controllers show similar performance during internal MMC faults. The reason for this is the internal implementation of

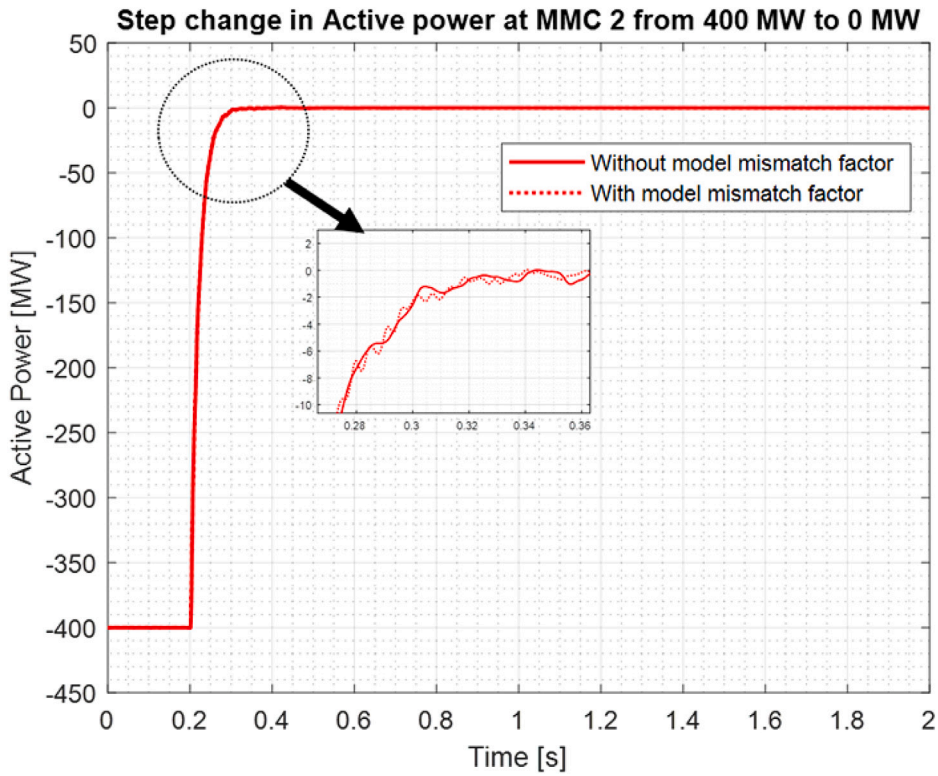

Fig. A.28. Comparison of the diagrams for the active power of the MMC 2 with and without model mismatch factor included.

the lower level controlling strategies for SM capacitor voltage balancing in RTDS and GTFPGAs.

Up to our knowledge, the proposed control and protection algorithms are implemented as a standalone for the first time together with controller interoperability and post DC fault performance of MPC.

Declaration of competing interest

The authors declare that they have no known competing financial interests or personal relationships that could have appeared to influence the work reported in this paper.

Data availability

No data was used for the research described in the article.

Acknowledgments

This project has been supported by the Dutch Ministry of Education, Culture and Science (OCW) through the Sector Plan Committee for Science and Technology project granted to the Technical University of Delft.

Appendix. Model mismatch factor

The mismatch between the model and plant can be handled by a factor called model mismatch factor. This factor considers the effect of any difference in the plant and model into the optimization problem. This mismatch factor is formulated as:

$$x(k+m|k) = C_d A_d^m x(k) + C_d \sum_{i=0}^{m-1} A^{m-i-1} B_d L(i)^T \eta + I_m e(k)$$
$$= F(m)x(k) + \phi(m)^T \eta + I_m e(k), \quad \text{(A.1)}$$

where $F(m) = C_d A_d^m$, $\phi(m)^T = C_d \sum_{i=0}^{m-1} A^{m-i-1} B_d L(i)^T$ and $m \in \{1, 2, \ldots, N_p\}$. The new term in the above formulation is the $I_m e(k)$ for I_m being an identity matrix of order $(5, 5)$ and $e(k)$ is error between the model output signal and plant output at time step k. Considering the cost function, J given Eq. (8) and substituting Eq. (A.1) in J and re-arranging terms we get:

$$H = \phi^T Q \phi + R, \quad \text{(A.2a)}$$

$$f = \phi^T Q[\overline{R(k)} - I_p e(k) - F x(k)], \quad \text{(A.2b)}$$

where H and f matrices are the input to QP optimization solver. The $\overline{R(k)} = \vec{1}_{1\times N_p} \otimes \vec{r}$, where $\vec{r}$ is the reference signal column matrix of order 5 at k instance and $\otimes$ is Kronecker Tensor Product. F and ϕ are evolution of $F(m)$ and $\phi(m)$ matrix over N_p with given system dynamics. The $I_p = [I_1, I_2, \ldots, I_{N_p}]^T$ and I_i, for $i \in \{1, 2, \ldots, N_p\}$, is an identity matrix of order $(5, 5)$, which acts like weight factor for the error mismatch. Following figure shows the impact of mismatch factor during the step change event.

For the simulated power system from Section 5, the time diagrams with and without mismatch factor are depicted in Fig. A.28 for the MMC 2. In this test case the active power has been changed from 400 MW to 0 MW.

References

[1] Moore JNM, Wagner A. D12.4 - Final Deployment Plan. 2020, 691714.

[2] Alavirad S, Mohammadi S, Golombok M, Haans K. Interconnection and generation from a North Sea power hub â€“ a linear electricity model. Int J Electr Power Energy Syst 2021;133:107132. http://dx.doi.org/10.1016/j.ijepes.2021.107132, URL: https://www.sciencedirect.com/science/article/pii/S0142061521003719.

[3] Itiki R, Di Santo SG, Itiki C, Manjrekar M, Chowdhury BH. A comprehensive review and proposed architecture for offshore power system. Int J Electr Power Energy Syst 2019;111:79–92. http://dx.doi.org/10.1016/j.ijepes.2019.04.008, URL: https://www.sciencedirect.com/science/article/pii/S014206151930095X.

[4] Moore J. D12.1 Preliminary analysis of key technical, financial, economic, legal, regulatory and market barriers and related portfolio of solutions. 691714, 2018, p. 82.

[5] Integration O. Detailed Specification of the Demostrator. 2016.

[6] IEEE. Stability definitions and characterization of dynamic behavior in systems with high penetration of power electronic interfaced technologies. Technical Report April Pes-Tr77, 2020, p. 1–42.

[7] Agbemuko AJ, Aa JDA-G, Prieto-Araujo E, Gomis-Bellmunt O. Dynamic modelling and interaction analysis of multi-terminal VSC-HVDC grids through an impedance-based approach. Int J Electr Power Energy Syst 2019;113:874–87. http://dx.doi.org/10.1016/j.ijepes.2019.06.029, URL: https://www.sciencedirect.com/science/article/pii/S0142061519300195.

[8] CIGRE Working Group B470. Guide for electromagnetic transient studies involving VSC converters. Technical report April, 2021.

[9] Jaladi KK, Sandhu KS. Real-time simulator based hybrid controller of DFIG-WES during grid faults design and analysis. Int J Electr Power Energy Syst 2020;116:105545. http://dx.doi.org/10.1016/j.ijepes.2019.105545, URL: https://www.sciencedirect.com/science/article/pii/S0142061518323950.

[10] Yushkova M, Sanchez A, de Castro A. Strategies for choosing an appropriate numerical method for FPGA-based HIL. Int J Electr Power Energy Syst 2021;132:107186. http://dx.doi.org/10.1016/j.ijepes.2021.107186, URL: https://www.sciencedirect.com/science/article/pii/S0142061521004257.

[11] Poblete P, Neira S, Aguilera RP, Pereda J, Pou J. Sequential phase-shifted model predictive control for modular multilevel converters. IEEE Trans Energy Convers 2021;36(4):2691–702. http://dx.doi.org/10.1109/TEC.2021.3074863.

[12] P. Martin S, Li H, M. Anubi O. Modulated MPC for arm inductor-less MVDC MMC with reduced computational burden. IEEE Trans Energy Convers 2021;36(3):1776–86. http://dx.doi.org/10.1109/TEC.2021.3069150.

[13] Wang S, Dragicevic T, Gao Y, Teodorescu R. Neural network based model predictive controllers for modular multilevel converters. IEEE Trans Energy Convers 2021;36(2):1562–71. http://dx.doi.org/10.1109/TEC.2020.3021022.

[14] Kong X, Wang X, Abdelbaky MA, Liu X, Lee KY. Nonlinear MPC for DFIG-based wind power generation under unbalanced grid conditions. Int J Electr Power Energy Syst 2022;134:107416. http://dx.doi.org/10.1016/j.ijepes.2021.107416, URL: https://www.sciencedirect.com/science/article/pii/S0142061521006554.

[15] Tao H, Peng T, Yang C, Gao J, Chen Z, Yang C, et al. An FCS-MPC-based open-circuit and current sensor fault diagnosis method for traction inverters with two current sensors. Int J Electr Power Energy Syst 2023;144:108526. http://dx.doi.org/10.1016/j.ijepes.2022.108526, URL: https://www.sciencedirect.com/science/article/pii/S0142061522005282.

[16] Fidai MH, Babazadeh D, Hanning J, Larsson T, Nordström L. Real-time implementation of optimal power flow calculator for HVDC grids. KTH, Industrial Information and Control Systems; 2015, QC 20150624. QC 20160212.

[17] Jeong M, Fuchs S, Biela J. When FPGAs meet regionless explicit MPC: An implementation of long-horizon linear MPC for power electronic systems. In: IECON 2020 the 46th annual conference of the ieee industrial electronics society. 2020, p. 3085–92. http://dx.doi.org/10.1109/IECON43393.2020.9254277.

[18] González-Torres I, Miranda H, Méndez-Barrios C-F, Espinoza J, Cárdenas V. Long-length horizons dynamic matrix predictive control for a MMC inverter. Electr Power Syst Res 2019;168:137–45. http://dx.doi.org/10.1016/j.epsr.2018.11.020, URL: https://www.sciencedirect.com/science/article/pii/S037877961830395X.

[19] Zhang F, Li W, Joós G. A voltage-level-based model predictive control of modular multilevel converter. IEEE Trans Ind Electron 2016;63(8):5301–12. http://dx.doi.org/10.1109/TIE.2016.2572671.

[20] Dong J, Jia M, Han Y, Geng Z, Zhong Y. An improved MPC integrating fuzzy PI of an MMC-HVDC system. In: 2019 IEEE 8th data driven control and learning systems conference. 2019, p. 471–6. http://dx.doi.org/10.1109/DDCLS.2019.8908849.

[21] Thau E, Kamal E, Marinescu B, Denis G. EMT implementation and validation of MPC for VSC-HVDC embedded in AC meshed grid. In: 2020 IEEE electric power and energy conference. 2020, p. 1–6. http://dx.doi.org/10.1109/EPEC48502.2020.9320020.

[22] Belhaouane MM, Almaksour K, Papangelis L, Colas F, Prevost T, Guillaud X, et al. Experimental validation of a model predictive control strategy on a three-terminal VSC-HVDC mock-up. In: 15th IET international conference on AC and DC power transmission. 2019, p. 1–6. http://dx.doi.org/10.1049/cp.2019.0093.

[23] Roose T, Lekić A, Alam MM, Beerten J. Stability analysis of high-frequency interactions between a converter and HVDC grid resonances. IEEE Trans Power Deliv 2020;1. http://dx.doi.org/10.1109/TPWRD.2020.3041176.

[24] Badrkhani Ajaei F, Iravani R. Dynamic interactions of the MMC-HVDC grid and its host AC system due to AC-side disturbances. IEEE Trans Power Deliv 2016;31(3):1289–98. http://dx.doi.org/10.1109/TPWRD.2015.2512178.

[25] Wenig S, Goertz M, Hirsching C, Suriyah M, Leibfried T. On full-bridge bipolar MMC-HVDC control and protection for transient fault and interaction studies. IEEE Trans Power Deliv 2018;33(6):2864–73. http://dx.doi.org/10.1109/TPWRD.2018.2823770.

[26] Sakinci OC, Lekić A, Beerten J. Generalized impedance-based AC/DC power system modeling for harmonic stability analysis. Int J Electr Power Energy Syst 2022;143:108456. http://dx.doi.org/10.1016/j.ijepes.2022.108456, URL: https://www.sciencedirect.com/science/article/pii/S0142061522004653.

[27] Han M, Nguyen P, Yan W. Inter-harmonics in multi-terminal VSC-based HVDC systems. J Mod Power Syst Clean Energy 2016;4(2):282–91. http://dx.doi.org/10.1007/s40565-015-0173-4.

[28] Lekić A, Beerten J. Generalized multiport representation of power systems using ABCD parameters for harmonic stability analysis. In: Electric power system research: proceedings of the 21st power systems computation conference, vol. 189. Elseiver; 2020, p. 7.

[29] Zhou M, Xiang W, Zuo W, Lin W, Wen J. A novel HVDC circuit breaker for HVDC application. Int J Electr Power Energy Syst 2019;109:685–95. http://dx.doi.org/10.1016/j.ijepes.2019.02.045, URL: https://www.sciencedirect.com/science/article/pii/S0142061518329107.

[30] Mirhosseini SS, Liu S, Muro JC, Liu Z, Jamali S, Popov M. Modeling a voltage source converter assisted resonant current DC breaker for real time studies. Int J Electr Power Energy Syst 2020;117:105678. http://dx.doi.org/10.1016/j.ijepes.2019.105678, URL: https://www.sciencedirect.com/science/article/pii/S0142061519324858.

[31] Bergna-Diaz G, Freytes J, Guillaud X, D'Arco S, Suul JA. Generalized voltage-based state-space modeling of modular multilevel converters with constant equilibrium in steady state. IEEE J Emerg Sel Top Power Electron 2018;6(2):707–25. http://dx.doi.org/10.1109/JESTPE.2018.2793159.

[32] Shetgaonkar A, Lekić A, Rueda Torres JL, Palensky P. Microsecond enhanced indirect model predictive control for dynamic power management in MMC units. Energies 2021;14(11). http://dx.doi.org/10.3390/en14113318.

[33] Qin J, Saeedifard M. Predictive control of a modular multilevel converter for a back-to-back HVDC system. IEEE Trans Power Deliv 2012;27(3):1538–47. http://dx.doi.org/10.1109/TPWRD.2012.2191577.

[34] Zhou D, Yang S, Tang Y. A voltage-based open-circuit fault detection and isolation approach for modular multilevel converters with model-predictive control. IEEE Trans Power Electron 2018;33(11):9866–74. http://dx.doi.org/10.1109/TPEL.2018.2796584.

[35] Böcker J, Freudenberg B, The A, Dieckerhoff S. Experimental comparison of model predictive control and cascaded control of the modular multilevel converter. IEEE Trans Power Electron 2015;30(1):422–30. http://dx.doi.org/10.1109/TPEL.2014.2309438.

[36] Dekka A, Wu B, Zargari NR. Minimization of DC-bus current ripple in modular multilevel converter under unbalanced conditions. IEEE Trans Power Electron 2017;32(6):4125–31. http://dx.doi.org/10.1109/TPEL.2016.2630921.

[37] Vatani M, Bahrani B, Saeedifard M, Hovd M. Indirect finite control set model predictive control of modular multilevel converters. IEEE Trans Smart Grid 2015;6(3):1520–9. http://dx.doi.org/10.1109/TSG.2014.2377112.

[38] Liu P, Wang Y, Cong W, Lei W. Grouping-sorting-optimized model predictive control for modular multilevel converter with reduced computational load. IEEE Trans Power Electron 2016;31(3):1896–907. http://dx.doi.org/10.1109/TPEL.2015.2432767.

[39] Moon J-W, Gwon J-S, Park J-W, Kang D-W, Kim J-M. Model predictive control with a reduced number of considered states in a modular multilevel converter for HVDC system. IEEE Trans Power Deliv 2015;30(2):608–17. http://dx.doi.org/10.1109/TPWRD.2014.2303172.

[40] Wang Y, Cong W, Li M, Li N, Cao M, Lei W. Model predictive control of modular multilevel converter with reduced computational load. In: 2014 IEEE applied power electronics conference and exposition. 2014, p. 1776–9. http://dx.doi.org/10.1109/APEC.2014.6803546.

[41] Huang J, Yang B, Guo F, Wang Z, Tong X, Zhang A, Xiao J. Priority sorting approach for modular multilevel converter based on simplified model predictive control. IEEE Trans Ind Electron 2018;65(6):4819–30. http://dx.doi.org/10.1109/TIE.2017.2774725.

[42] Mahmoudi H, Aleenejad M, Ahmadi R. Modulated model predictive control of modular multilevel converters in VSC-HVDC systems. IEEE Trans Power Deliv 2018;33(5):2115–24. http://dx.doi.org/10.1109/TPWRD.2017.2727478.

[43] Nowak T, Suriyah M, Leibfried T. Power tracking in a MMC-multi-terminal HVDC system with centralized and decentralized MPC using a black box modeling approach. In: 2017 52nd international universities power engineering conference. 2017, p. 1–4. http://dx.doi.org/10.1109/UPEC.2017.8232017.

[44] Zhang J, Hu Z, Tian X. Research on MMC-HVDC multi-objective model predictive control strategy under asymmetric faults. Energy Rep 2020;6:430–9. http://dx.doi.org/10.1016/j.egyr.2020.11.218, URL: https://www.sciencedirect.com/science/article/pii/S2352484720316449, 2020 The 7th International Conference on Power and Energy Systems Engineering.

[45] Pirooz Azad S, Iravani R, Tate JE. Damping inter-area oscillations based on a model predictive control (MPC) HVDC supplementary controller. IEEE Trans Power Syst 2013;28(3):3174–83. http://dx.doi.org/10.1109/TPWRS.2013.2247640.

[46] Mc Namara P, Negenborn RR, De Schutter B, Lightbody G, McLoone S. Distributed MPC for frequency regulation in multi-terminal HVDC grids. Control Eng Pract 2016;46:176–87. http://dx.doi.org/10.1016/j.conengprac.2015.11.001, URL: https://www.sciencedirect.com/science/article/pii/S0967066115300423.

[47] Wang L. Model predictive control system design and implementation using MATLAB®. Springer Science & Business Media; 2009.

[48] Huang L, Xin H, Wang Z, Wu K, Wang H, Hu J, et al. A virtual synchronous control for voltage-source converters utilizing dynamics of DC-link capacitor to realize self-synchronization. IEEE J Emerg Sel Top Power Electron 2017;5(4):1565–77. http://dx.doi.org/10.1109/JESTPE.2017.2740424.

[49] Zhang Z, Chen W, Zhang Z. A New Seamless Transfer Control Strategy of the Microgrid. Sci World J 2014;2014:391945. http://dx.doi.org/10.1155/2014/391945.

[50] Dekka A, Wu B, Yaramasu V, Fuentes RL, Zargari NR. Model predictive control of high-power modular multilevel converters—An overview. IEEE J Emerg Sel Top Power Electron 2019;7(1):168–83. http://dx.doi.org/10.1109/JESTPE.2018.2880137.

[51] Maguire T, Warkentin B, Chen Y, Hasler J. Efficient techniques for real time simulation of MMC systems. In: Proc. int. conf. power syst. transients. 2013, p. 1–7.

[52] Cigré WG. B4. 57."Guide for the development of models for HVDC converters in a HVDC grid". CIGRE Technical Brochure, 604, 2014.

[53] IEEE WG 150809. Modeling and Analysis of System Transients Using Digital Programs. Technical report IEEE Pes, 1998, p. 87.

[54] Liu S, Popov M, Mirhosseini SS, Nee S, Modeer T, Ängquist L, et al. Modeling, experimental validation, and application of VARC HVDC circuit breakers. IEEE Trans Power Deliv 2020;35(3):1515–26. http://dx.doi.org/10.1109/TPWRD.2019.2947544.

[55] Liu S, Shetgaonkar A, Popov M. Coordinative performance of HVDC circuit breakers in MTDC grids. In: 2020 IEEE power energy society general meeting. 2020, p. 1–5. http://dx.doi.org/10.1109/PESGM41954.2020.9281921.

[56] Shetgaonkar A, Liu S, Popov M. Comparative analysis of a detailed and an average VARC DCcb model in MTDC systems. In: 2022 IEEE power energy society general meeting. 2022, p. 1–5.

[57] Yazdani A, Iravani R. A neutral-point clamped converter system for direct-drive variable-speed wind power unit. IEEE Trans Energy Convers 2006;21(2):596–607.

[58] Shariatpanah H, Fadaeinedjad R, Rashidinejad M. A new model for PMSG-based wind turbine with yaw control. IEEE Trans Energy Convers 2013;28(4):929–37. http://dx.doi.org/10.1109/TEC.2013.2281814.

[59] RTDS Technologies Inc. VSC small time-step turorial of RTDS user manuals. Technical report, 2013, p. 4–48.

[60] Weather file. 2022, https://weatherfile.com/. [Accessed 08 December 2021].

[61] Lindén K, Beerten J, Alvarez A, Barker C, Hanson J, Iravani R, et al. Control methodologies for direct voltage and power flow in a meshed HVDC Grid. Technical report 294 Electra, 2017, p. 72–5.